CHAPTER 2

Proton Exchange Membrane Fuel Cells

Adam Z. Weber,* **Sivagaminathan Balasubramanian,** and **Prodip K. Das**

Contents

1. Introduction 66
2. Fundamentals of Fuel Cells 70
   - 2.1 Thermodynamics 71
   - 2.2 Kinetics 74
   - 2.3 Conservation and transport 79
3. Modeling Aspects of Fuel Cells 88
   - 3.1 Membrane 89
   - 3.2 Porous media 99
   - 3.3 Catalyst layers 111
   - 3.4 Gas flow channels and flowfields 118
   - 3.5 Boundary conditions and summary 122
   - 3.6 Impedance modeling 123
4. Optimization 124
   - 4.1 Single-parameter optimization 125
   - 4.2 Multiparameter optimization 131
5. Summary 136

Acknowledgments 141
References 142

Abstract Proton-exchange membrane fuel cells are promising devices for a variety of energy-conversion technologies. However, they have limited market penetration due to their high cost, which stems from the

Environmental Energy Technologies Division, Lawrence Berkeley National Laboratory, Berkeley, California, USA
* Corresponding author, E-mail address: azweber@lbl.gov

Advances in Chemical Engineering, Volume 41
ISSN 0065-2377, DOI: 10.1016/B978-0-12-386874-9.00003-8

need to balance durability, performance, and materials. To understand and quantify these complex interactions, detailed mathematical modeling of the underlying physical phenomena is an ideal tool to describe the multiphysics. Similarly, to control the overall operation of the cell requires detailed mathematical models. In this chapter, we describe how one can model the dominant interactions and phenomena within a cell. These interactions involve several simultaneous processes including ionic resistance, gas- and liquid-phase transport, and catalytic reactions. To design and control fuel cells for efficient operation, an understanding of the interdependence of these processes across the layers of diffusion media, catalyst, and membrane is necessary, and the phenomena within each layer will be described in this chapter. In addition, current issues in the modeling of fuel cells including optimization of transport phenomena and multiphase flow, durability, and electrode structure will be introduced. The mathematical techniques and descriptions discussed in this chapter will aid scientists and engineers in understanding and designing fuel cells for various operating scenarios.

1. INTRODUCTION

Fuel cells efficiently convert chemical energy of a fuel into usable electrical energy through electrochemical reactions. Among the different types, polymer-electrolyte fuel cells (PEFCs) receive the most attention for automotive and small stationary applications because of their higher electrical efficiency, power density, and durability. In a PEFC, fuel—typically hydrogen—and oxygen from air are combined electrochemically across a solid polymer membrane generating electricity, water, and heat. The operation of a PEFC involves a complex overlap of interrelated physicochemical processes, which include electrochemical reactions as well as transport of ions, electrons, energy, and species in gas and liquid phases across a heterogeneous media. Though PEFCs have shown promising performance improvement in terms of efficiency and durability over the past three decades, the level of robustness required for operation in widely varying conditions, while matching the current power sources in terms of cost, stifles the commercial utilization of PEFCs. Any further improvements could be greatly aided by a better understanding of the complex processes of fuel-cell operation. Only through fundamental modeling based on physical models developed from experimental observations can the processes and operation of a PEFC be truly understood. Most of the discussion in this chapter focuses on proton-exchange-membrane fuel cells (PEMFC), although a brief mention is also made on anion-exchange-membrane fuel cells (AEMFCs).

A schematic of a typical PEMFC is shown in Figure 1. The polymer-electrolyte membrane is considered to be the heart of a PEMFC; it conducts ions and inhibits electron transfer from one electrode or catalyst layer to the other. The catalyst layers are complex structures typically composed of precious metals like Pt or Pt-alloy nanoparticles supported on porous carbon and ionomer (dispersed polymer-electrolyte tendrils). The complex structure provides pathways for the transport of reactant and product species, electrons, and protons to and from the active sites, where the electrochemical reactions take place. One of the electrode layers is referred to as anode, where the fuel oxidation takes place, and the other as cathode,

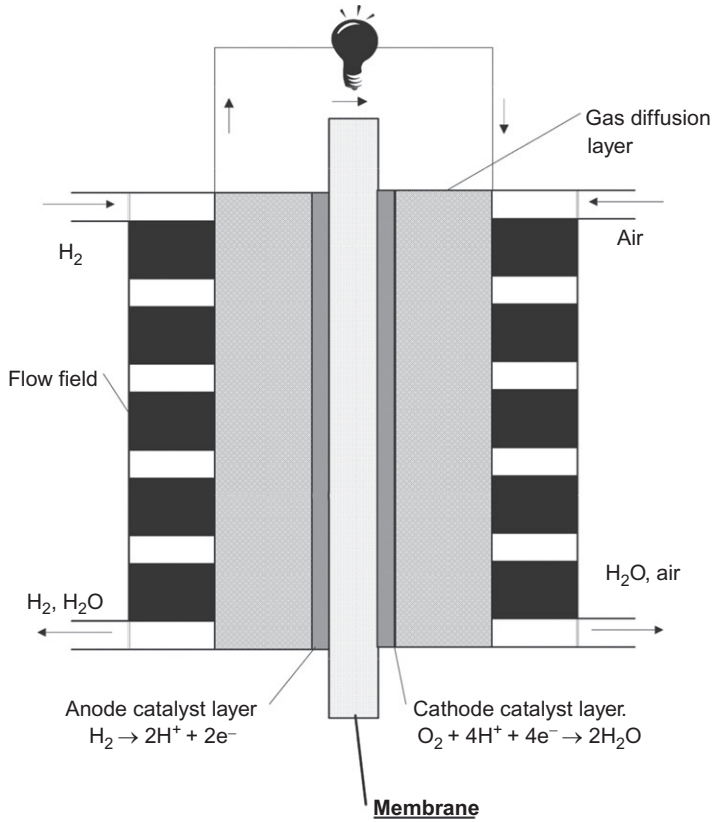

Figure 1 Schematic of a PEMFC showing the various critical layers or domains. Typical full-cell areas are on the order of 300 cm^2, and average dimensions for the membrane, catalyst layers, microporous layers, and gas-diffusion layers and flow channels are 20, 10, 40, 200, and 1000 μm, respectively.

where the reduction reaction takes place. If hydrogen is used as the fuel, it oxidizes at the anode releasing protons and electrons according to

$$H_2 \rightarrow 2H^+ + 2e^- \tag{1}$$

The generated protons are transported across the membrane and the electrons across the external circuit. At the cathode catalyst layer, the protons and electrons recombine with oxygen to generate water

$$4H^+ + 4e^- + O_2 \rightarrow 2H_2O \tag{2}$$

Although the above electrode reactions are written in single step, multiple elementary reaction pathways are possible at each electrode, a discussion of which is beyond the scope of this chapter. To distribute the gaseous hydrogen and oxygen across the electrodes as well as close the circuit for the flow of electrons, the membrane and electrodes are sandwiched between graphite blocks with gas flow channels and porous diffusion media or transport layers made of carbon and often composed of a macroporous gas-diffusion layer and a microporous layer next to the catalyst layer (see Figure 1).

The electrical energy of electrons that are transported through the external circuit can be used for powering devices. The electrical power, P (energy per unit time), generated by a fuel cell is the product of cell potential, V (energy per electron transported), and current, I (number of electrons transported per unit time),

$$P = V \times I \tag{3}$$

While the thermodynamics of the reactions dictates the maximum potential that any fuel cell can deliver, the current is limited by the kinetics and transport limitations within the cell. For every electron transported across the external circuit, an equal amount of charged species, that is, protons in PEMFC case, has to be generated, transported, and consumed between anode and cathode. It is during this transport that most of the losses occur. To maximize the power output, the engineers' task is to minimize the losses and maximize the current generation, which can be aided by modeling of the underlying physical phenomena.

The performance of a fuel cell is often reported as a polarization curve which demonstrates the steady-state potential/current relationship (Figure 2). The maximum free energy stored in the fuel is denoted as the equilibrium potential. A typical real-world polarization curve of a PEMFC has three distinct regions, where the change in overall performance is dominated by different phenomena. At low current densities, the behavior of a PEMFC is dominated by kinetic losses at the electrodes, which mainly stem from the high activation overpotential (i.e., excess energy spent to initiate reaction) of the oxygen-reduction reaction (ORR) at the cathode catalyst layer. As the current is increased, resistive losses become a

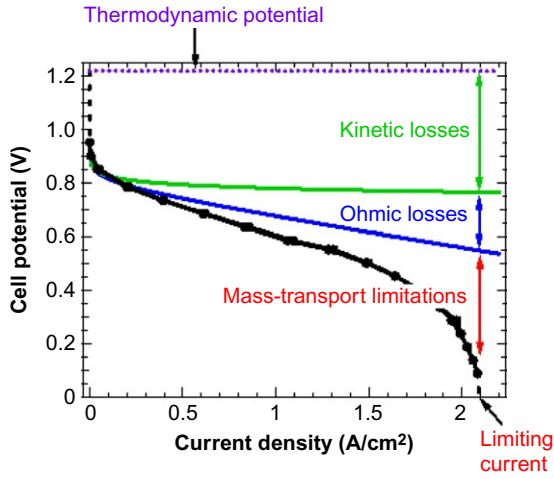

Figure 2 Example polarization curve showing a breakout of the dominant-loss regimes.

significant factor in lowering the overall cell potential. For this region, the resistance is essentially constant, that is, it is not a strong function of the potential, thus allowing for Ohm's law to be used for modeling purposes,

$$\Delta\Phi = iR' \tag{4}$$

where R' is the overall resistance, i is the current density (relative to the geometric membrane or active area), and Φ denotes the electronic potential. This region of the polarization curve is referred to as the ohmic region. These resistive losses are mainly from ionic losses in the electrodes and membrane, although contact and electronic resistances may be important under certain operating conditions or cell configurations. At high current densities, mass-transport limitations become increasingly important. These losses are because the rate of consumption of reactants at the catalytic sites exceeds that of the transport of reactants. In a typical PEMFC, oxygen transport to the cathode is limiting due to the use of air and the flooding of the cathode side of the cell by liquid water, but protons may also result in mass-transfer limitations, especially under dry operating conditions.

One can model or curve-fit the polarization behavior using a single equation without any reference to the geometry of the cell, hence it is zero-dimensional (0D). The 0D modeling equations can be derived by combination of the governing equations for each regime. A typical expression for this type of analysis is to relate the cell potential (V) with current as

$$V = U^{\theta} - b\log(i) - R'i + b\log\left(1 - \frac{i}{i_{\text{lim}}}\right) \tag{5}$$

In the above equation, the first term (U^{θ}) corresponds to the thermodynamic free-energy potential (see Figure 2); the second term accounts for the losses due to kinetics at the electrode, where b is the so-called Tafel slope and can be fitted to the data; the third term corresponds to the resistive losses as shown in Equation (4); and the last term corresponds to the mass-transport limitations where the limiting current (i_{lim}) is used. While such equations can be used to fit the polarization data, they are inadequate for predicting performance and truly explaining the underlying processes. However, the equation does cover the general losses in the cell.

Fuel-cell models vary widely and can be classified based on approaches like dimensionality, type of operation like steady state or transient, and region-specific models that focus on particular components like the membrane or cathode catalyst layer. Aforementioned 0D models are mainly empirical and simulate the polarization performance of a PEMFC with a simple equation. The 1D approach treats the PEMFC as a sandwich of components as seen in Figure 1. The majority of these models describe the different regions of the PEMFC sandwich using everything from simple equations to complex expressions derived from physical models. The 2D models deal with phenomena in a PEMFC that occur in the sandwich as well as in another direction, either across or along the gas channel. Across-the-channel 2D models account for rib and channel effects, while along-the-channel approaches account for concentration and phase change of species down the flow channels. Finally, the 3D models include the 1D sandwich and consider effects in both directions of the flowfield. In this chapter, we summarize the mathematical approaches used for the various phenomena. In addition, some of the areas of continuing research interest as well as general modeling results and performance optimizations are examined.

2. FUNDAMENTALS OF FUEL CELLS

A rigorous description of fuel-cell operation requires the coupling of thermodynamics and kinetics of the reactions and conservation of species, energy, and momentum within a representative geometry. In this section, the basic thermodynamic relations are discussed first, then kinetic relations are introduced, and finally various losses due to transport are explored.

2.1 Thermodynamics

A PEFC converts the intrinsic chemical energy of a fuel into electrical and heat energies. One can envision the cell as a black box or engine. From the first law of thermodynamics,

$$\Delta H = Q - W_s \tag{6}$$

one sees that the net release of energy is in the form of heat (Q) or work (W_s). The work performed by the system is simply the power as expressed by Equation (3). The net energy due to the electrochemical reaction is the difference between the heat of formation (H^f) of the products and reactants,

$$\Delta H = H^f_{H_2O} - \frac{1}{2}H^f_{O_2} - H^f_{H_2} \tag{7}$$

This enthalpy can be converted to an electrochemical potential, resulting in the enthalpy potential,

$$U_H = \frac{\Delta H}{z_i F} \tag{8}$$

where z_i is the charge number of species i and F is Faraday's constant. Using Equation (6), the expression for the heat released becomes

$$Q = i(U_H - V) \tag{9}$$

where V is the cell potential. Thus, if the cell potential equals the enthalpy potential, there is no net heat loss, which is why the enthalpy potential is often termed the thermoneutral potential. However, the enthalpy energy is not fully accessible as it is composed of both reversible or entropic ($Q_{rev}=T\Delta S$) and irreversible components. The maximum energy that is convertible to electrical energy is related to the free energy of the fuel,

$$\Delta G = \Delta H - T\Delta S \tag{10}$$

The potential corresponding to the Gibbs free energy is defined as the equilibrium potential,

$$U^\theta = \frac{\Delta G}{z_i F} \tag{11}$$

Usually, the fuel cell is operated at a temperature greater than the standard temperature of 25°C. This needs to be accounted for when estimating the thermodynamic properties of the system. Combining Equations (10) and (11) and differentiating with respect to temperature, the change in equilibrium potential is obtained as,

$$U = U^\theta + \Delta U = U^\theta + \frac{\Delta S}{z_i F}\left(T - T^\theta\right) \tag{12}$$

For hydrogen and oxygen becoming water, the enthalpy and equilibrium potentials are shown in Figure 3 as calculated from handbooks (Perry and Green, 1997; Weast, 1979). Depending on if the product water is vapor or liquid, one arrives at different potentials due to the latent heat and free-energy difference between liquid and vapor water. Thus, as the cell temperature increases, the amount of usable work from the fuel decreases (assuming the generated heat is expelled to the atmosphere), while the amount of heat generated increases for a given operating potential. Also, Figure 3 clearly shows how significant the latent heat of water can be (~200 mV), which can play an important role in terms of phase-change-induced flow as well as heat sources and sinks within the cell as described in later sections in this chapter.

At constant temperature, the change in Gibbs free energy is related to the change in system pressure as,

$$\Delta G = \overline{V}\Delta p \tag{13}$$

where $\overline{V}$ is the partial molar volume. Using the ideal-gas law,

$$p\overline{V} = RT \tag{14}$$

where R is the ideal-gas constant; the equilibrium potential can be written in terms of the local pressure (p_i) of the reactants and products at the electrode, which is known as the Nernst relation,

$$U = U^{\theta} - \frac{RT}{z_i F}\ln\left(\prod p_i^{s_i}\right) \tag{15}$$

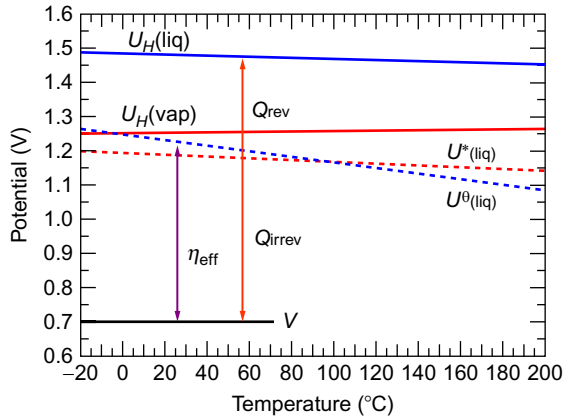

Figure 3 Thermodynamic potentials and definitions of a hydrogen fuel cell, where the heat lost (Q) is composed of reversible and irreversible losses and the cell is operating at a potential V.

where s_i is the stoichiometry of species i; the activity of the species is assumed to be approximated by the local concentration of the species. For the hydrogen fuel cell, the Nernst equation can be written as

$$U = U^{\theta} - \frac{RT}{2F}\ln\left(\frac{p_{H_2}\sqrt{p_{O_2}}}{p_{H_2O}}\right) \tag{16}$$

From examination of Equation (16), one can see that the two equilibrium potentials in Figure 3a are related by the vapor pressure of water, $p_{H_2O}^{vap}$

$$U^{\theta} = U^{*} + \frac{RT}{4F}\ln\left[\left(\frac{1}{p_{H_2O}^{vap}}\right)^2\right] \tag{17}$$

As noted above, when current flows, the available energy or potential of the cell decreases (see Figure 2) due to the losses in the cell. Thus, the net heat lost from the cell is

$$Q_{loss} = Q_{rev} + Q_{irrev} = i\left(U^{H} - U^{\theta}\right) + i\left(U^{\theta} - V\right) \tag{18}$$

which is summarized in Figure 3. Thus, if the cell operates at a potential between the equilibrium and enthalpy potentials, the process is endothermic; whereas if the operating potential is above the enthalpy potential or below the equilibrium potential, the process is exothermic. Also as shown in Figure 3, for PEMFCs, the efficiency of the cell, η_{eff}, is typically defined relative to the maximum free energy available for electrical work,

$$\eta_{eff} = 1 - \frac{V}{U} \tag{19}$$

One must also be cognizant of whether the efficiency is defined in terms of the equilibrium or enthalpy values, and what the reference state is for the calculation (i.e., vapor or liquid water). This is especially important when comparing different fuel cells as well as with fuel cells to other systems. For example, solid-oxide fuel cells operate at temperatures (600–900°C) where the heat generated can be recovered to electrical energy, thereby making efficiency greater than 100% possible using the definition above. Thus, it is advisable to use heating-value, enthalpy or enthalpy potential of the fuel as a metric for efficiency estimation. This allows for a better comparison with other technologies (e.g., combustion engines to fuel cells).

2.2 Kinetics

Thermodynamics dictates the maximum electrical potential available from a fuel cell. However, as noted above and in Figure 2, the major inefficiency in a PEMFC that brings down the cell potential is related to the kinetics of the reaction. The kinetic rate controls the generation of current in the fuel-cell electrodes. A typical electrochemical reaction at the electrode can be generally expressed as

$$\sum_k \sum_i s_{i,k,h} M_i^{z_i} \rightarrow n_h \mathrm{e}^- \tag{20}$$

where $s_{i,k,h}$ is the stoichiometric coefficient of species i residing in phase k and participating in electron-transfer reaction h, n_h is the number of electrons transferred in reaction h, and M_i represents the chemical formula of species i, and z_i its valence. Equations (1) and (2) are specific forms for the anode and cathode reactions occurring in a PEMFC.

As defined before, the current is the rate of transport of electrons across the external circuit and an equivalent ionic charge is transferred between electrodes (i.e., through the membrane). The ion transfer rate is equal to the electrochemical reaction rate at the electrodes. According to Faraday's law, the flux or species i in phase k and rate of reaction h is related to the current as

$$N_{i,k} = \sum_h r_{h,i,k} = \sum_h s_{i,k,h} \frac{i_h}{n_h F} \tag{21}$$

where i_h refers to current density, that is, current (i) per unit geometric area of the electrode. The rate of a chemical reaction is related to its concentration and temperature through an Arrhenius relationship,

$$r_h = k \exp\left(\frac{-E_\mathrm{a}}{RT}\right) \prod_i \left(\frac{c_i}{c_i^{\mathrm{ref}}}\right)^{m_i} \tag{22}$$

where k is the rate constant, m_i is the order of reaction for species i, and c_i is the concentration of the reactant i. The concentration term may be written in terms of partial pressure (p_i) for gaseous species or activity (a_i) for solution species. For the reaction, there is always resistance which must be overcome. E_a is the activation energy required to overcome the resistance and the reaction. The spontaneity of the reaction is inversely proportional to the activation energy required, which may be partially offset by increasing the temperature or concentration of reacting species. For an electrochemical reaction, the rate depends as well on the potential drop across the reaction interface between phases k and p, which are normally the electrode and electrolyte, respectively. Relating the above

equations with the definition of Gibbs free energy, the rate of a reversible electrochemical reaction can be written as

$$i_{h,k-p} = i_{0_h}\left[\prod_i^a \left(\frac{p_i}{p_i^{\text{ref}}}\right)^{m_i} \exp\left(\frac{\alpha_a n_h F \eta_{h,k-p}}{RT}\right) - \prod_i^c \left(\frac{p_i}{p_i^{\text{ref}}}\right)^{m_i} \exp\left(\frac{-\alpha_c n_h F \eta_{h,k-p}}{RT}\right)\right] \tag{23}$$

where i_h is the transfer current between phases k and p due to electron-transfer reaction h; the two terms within the brackets correspond to the forward and reverse reactions and thus the products are over the anodic and cathodic reaction species, respectively; α_a and α_c are the anodic and cathodic transfer coefficients, respectively (often determined empirically for multistep reactions); p_i and p_i^{ref} are the partial pressure and reference partial pressure for species i; and m_i is the order of reaction for reactant i. The above equation is called the Butler–Volmer equation. In the above expression, the composition-dependent part of the exchange current density is explicitly written, with the multiplication over those species in participating in the anodic or cathodic direction. The activation overpotential ($\eta_{h,k-p}$) is defined as the difference in potential between phases electrode and electrolyte with respect to a reference electrode potential (U_h^{ref}) for reaction h.

$$\eta_h = \Phi_k - \Phi_p - U_h^{\text{ref}} \tag{24}$$

The reference potential can be determined using a Nernst equation (e.g., see Equation (16)); if the reference conditions are the same as the standard conditions (i.e., 100 kPa pressure for the different gas species), then U_h^{ref} has the same numerical value as U^θ. In this chapter, the reference electrode used is defined as a platinum metal electrode exposed to hydrogen at the same temperature and electrolyte (e.g., Nafion®) as the solution of interest. With this reference electrode, the electrode overpotential defined in Equation (24) is the same as having the reference electrode located next to the reaction site but exposed to the reference conditions (i.e., it carries its own extraneous phases with it). Typical values for the reference conditions are those in the gas channels. If the reference electrode is exposed to the conditions at the reaction site, then a surface or kinetic overpotential can be defined as

$$\eta_{s_h} = \Phi_k - \Phi_p - U_h \tag{25}$$

where U_h is the reversible potential of reaction h. The surface overpotential is the overpotential that directly influences the reaction rate across the interface. Comparing Equations (25) and (24), one can see that the electrode overpotential contains both a concentration and a surface

overpotential for the reaction; the reader is referred to Neyerlin *et al.* (2006) for a very good discussion of the different overpotentials.

Unlike for chemical reactions, electrochemical reactions offer the leverage of potential with which the reaction rate can be controlled as shown in Equation (23) and Figure 4. The reaction diagram clearly shows the impact of potential in lowering the energy barriers for the reaction to proceed, and it gives a visualization of the overpotential effects. By leveraging the overall cell potential, the direction and rate of reaction can be controlled. It should be noted that the Butler–Volmer equation is relatively general and often taken to be empirical. The equation is exact for a single elementary reaction rate and the dependence of the exchange current density and the reaction rates on concentration, etc., can be derived. However, for multiple reaction steps and mechanisms, this becomes cumbersome and requires detailed knowledge of the reaction mechanism (Newman and Thomas-Alyea, 2004). For the PEMFC reactions, the Butler–Volmer equation is often used and the various dependences and values determined empirically since both reactions can have multiple steps, depend on catalysts used, etc.; such detailed discussion is beyond the scope of this chapter and the reader is referred to various books on this subject (Newman and Thomas-Alyea, 2004; Wieckowski, 2009).

For the hydrogen-oxidation reaction (HOR) occurring at the porous anode catalyst layer (see Equation (1)), Equation (23) can be written as

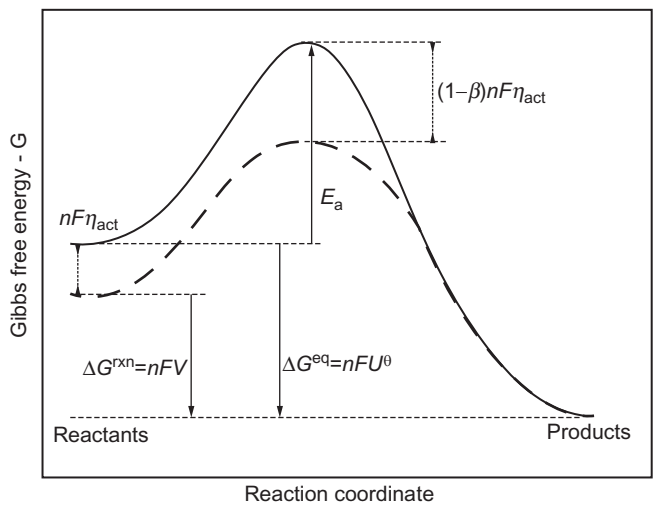

Figure 4 Reaction diagram showing the impact of the potential on an elementary electrochemical reaction.

$$i_{\mathrm{HOR}} = i_{0_{\mathrm{HOR}}}\left[\frac{p_{\mathrm{H_2}}}{p_{\mathrm{H_2}}^{\mathrm{ref}}}\exp\left(\frac{\alpha_{\mathrm{a}}F}{RT}(\eta_{\mathrm{HOR}})\right) - \left(\frac{a_{\mathrm{HM}}}{a_{\mathrm{HM}}^{\mathrm{ref}}}\right)^2\exp\left(\frac{-\alpha_{\mathrm{c}}F}{RT}(\eta_{\mathrm{HOR}})\right)\right] \quad (26)$$

where 1 and 2 denote the electron- and proton-conducting phases, respectively, and the reaction is almost always taken to be first order in hydrogen. Typically, the dependence on the activity of the proton(H)–membrane(M) complex is not shown, as the electrolyte is a polymer of defined acid concentration (i.e., $a_{\mathrm{HM}}=a_{\mathrm{HM}}^{\mathrm{ref}}$). However, if one deals with contaminant ions, then Equation (26) should be used as written. Also, it has recently been shown that the HOR may proceed with a different mechanism at low hydrogen concentrations; in this case, the kinetic equation is altered through the use of a surface adsorption term (Wang *et al.*, 2006). Due to the choice of reference electrode, the reference potential and reversible potential are both equal to zero.

If the system is at equilibrium, then the rate of the forward reaction is equal to the rate of the reverse reaction, that is, the net current is zero and the Nernst equation (16) is obtained for an elementary reaction. The reaction rates at this equilibrium are written as a current density (the exchange current density) and is defined as

$$i_{0_{\mathrm{HOR}}} = i_{0_{\mathrm{HOR}}}^{\mathrm{ref}}\mathrm{AL}\,\exp\left(\frac{-E_{\mathrm{a}}}{RT}\left[1-\frac{T}{T^{\mathrm{ref}}}\right]\right) \quad (27)$$

where $i_{0_{\mathrm{HOR}}}{}^{\mathrm{ref}}$ refers to the exchange current density at the reference conditions and is based on the catalyst surface area (e.g., platinum). To change this from per unit catalyst area to geometric area, a roughness factor, AL, is used (i.e., $\mathrm{cm}^2_{\mathrm{geo}}/\mathrm{cm}^2_{\mathrm{Pt}}$). The exchange current density of a reaction is an indicator of the ease of the reaction. The exchange current density for the HOR reaction depends on catalyst being used and is very high ($\sim 1\,\mathrm{mA/cm^2}$) for platinum, which is the typical catalyst of choice (Neyerlin *et al.*, 2007).

Unlike the facile HOR, the ORR is slow. Due to its sluggishness, the anodic part of the ORR is considered negligible and is dropped, resulting in the so-called Tafel approximation

$$i_{\mathrm{ORR}} = -i_{0_{\mathrm{ORR}}}\left(\frac{p_{\mathrm{O_2}}}{p_{\mathrm{O_2}}^{\mathrm{ref}}}\right)^{m_0}\left(\frac{a_{\mathrm{HM}}}{a_{\mathrm{HM}}^{\mathrm{ref}}}\right)^2\exp\left(\frac{-\alpha_{\mathrm{c}}F}{RT}(\eta_{\mathrm{ORR}})\right) \quad (28)$$

with a dependence on oxygen partial pressure, m_0, of between 0.8 and 1 (Appleby, 1970; Kinoshita, 1992; Neyerlin *et al.*, 2006; Parthasarathy *et al.*, 1992a) and the same Arrhenius temperature dependence as seen in Equation (27). For both the HOR and ORR, α is typically taken to be equal to 1 (Appleby, 1970; Neyerlin *et al.*, 2006, 2007; Parthasarathy *et al.*, 1992b; Uribe *et al.*, 1992); however, newer models

use a value much closer to 0.5 for the ORR due to Pt-oxide formation (Wang *et al.*, 2007).

The four-electron ORR involves oxide formation, which forms at the potential range of the ORR (0.6–1.0 V) by water- or gas-phase oxygen. These oxides can inhibit the ORR by blocking active Pt sites with chemisorbed surface oxygen. Typically, a constant Tafel slope for the ORR kinetics around 60–70 mV/decade is assumed over the cathode potential range relevant to PEMFC operation. However, it has been suggested by experiments that this approach has to be modified to account for the potential-dependent oxide coverage (Caremans *et al.*, 2010; Gottesfeld, 2008; Wang *et al.*, 2007). To implement this coverage, a term is added to the ORR kinetic Equation (28) (Stamenkovic *et al.*, 2007),

$$i_{\mathrm{ORR}} = -i_{0_{\mathrm{ORR}}}(1-\Theta_{\mathrm{PtO}})\left(\frac{p_{\mathrm{O_2}}}{p_{\mathrm{O_2}}^{\mathrm{ref}}}\right)^{m_0}\left(\frac{a_{\mathrm{HM}}}{a_{\mathrm{HM}}^{\mathrm{ref}}}\right)^{4}\exp\left(\frac{-\alpha_{\mathrm{c}}F}{RT}(\eta_{\mathrm{ORR}})\right) \tag{29}$$

where Θ_{PtO} is the coverage of Pt oxide; it should be noted that several oxides can exist and here PtO is taken as an example. To calculate Θ_{PtO}, one can write a Butler–Volmer expression (see Equation (23)) for the formation of the surface oxide and solve it under a pseudo-steady-state approximation to yield

$$\Theta_{\mathrm{PtO}} = \frac{\exp\left[\frac{\alpha'_{\mathrm{a}}F}{RT}\eta_{\mathrm{PtO}}\right]}{\exp\left[\frac{\alpha'_{\mathrm{a}}F}{RT}\eta_{\mathrm{PtO}}\right]+\exp\left[\frac{-\alpha'_{\mathrm{c}}F}{RT}\eta_{\mathrm{PtO}}\right]} \tag{30}$$

where

$$\eta_{\mathrm{PtO}} = \Phi_1 - \Phi_2 - U_{\mathrm{PtO}} \tag{31}$$

and η_{PtO} and U_{PtO} are the Pt-oxide overpotential and equilibrium potential, respectively. Figure 5 shows the coverage of Pt oxide as a function of cell potential, and one can see that the influence of the oxide is to decrease the ORR rate at higher potentials and essentially make the Tafel slope become potential dependent.

While the ORR and HOR are the principal reactions occurring in PEMFCs, it is worth noting the possibility of side reactions. These reactions stem from durability and degradation analyses and are not covered in this chapter, although durability is addressed in Chapter 5. One of these other reactions is a two-electron reduction of oxygen crossing over from the cathode to the anode to form hydrogen peroxide (Liu and Zuckerbrod, 2005). In addition, hydrogen peroxide also forms at the cathode as part of the ORR (Paulus *et al.*, 2001). Also, hydrogen in the membrane that is crossing over can reduce platinum ions to metal, forming a platinum band in the membrane (Burlatsky *et al.*, 2006). The formation of Pt-oxide as described above also creates a

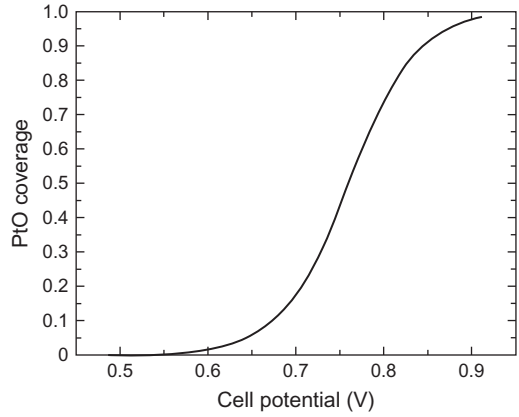

Figure 5 Formation of Pt-oxide as a function of cell potential (Yoon and Weber, 2011).

situation where in the Pt can dissolve during the transition at moderate potentials before significant oxide has formed to protect it from dissolution (Darling and Meyers, 2003, 2005). Finally, oxygen evolution (the anodic term to the ORR equation) and carbon oxidation at the cathode can also occur due to fuel starvation at the anode (Meyers and Darling, 2006; Reiser *et al.*, 2005).

2.3 Conservation and transport

Transport processes occurring within a PEMFC can be represented by coupling conservation equations for mass, momentum, energy, and charge transport within various subdomains constrained within reasonable boundary conditions. In this section, the general conservation laws are presented along with the general transport equations. Later in this chapter, specific relations that link physical properties within the various subdomain classes are discussed.

A general conservation equation can be written as

$$\frac{\partial \psi}{\partial t} + \nabla \cdot N_{\psi} = S_{\psi} \tag{32}$$

where the variable ψ corresponds to any variable or property that is conserved within the control domain. The first term corresponds to the rate of accumulation of ψ and the second term to the contribution from the flux (N) of ψ, while the third term, S_{ψ}, corresponds to the source term for ψ. For steady-state operation or assumption, where there is no time-dependent change in ψ, the first term can be neglected. Also, depending on the type of physical quantity and subdomain in which

the system is solved, the flux and source terms can be split into multiple contributing components. Transport through porous structures and all of the domains in this chapter is from a macrohomogeneous perspective using volume-averaged conservation equations.

2.3.1 Material

The conservation of material can be written as in Equation (32) except that the physical quantity ψ could be p—partial pressure of gas, c—concentration of solution, x—mole fraction of particular species, or ρ—density of fluid. However, for the case of a mixture in a multiphase system, it is necessary to write material balances for each of the component in each phase k, which in summation can still govern the overall conservation of material,

$$\frac{\partial \varepsilon_k c_{i,k}}{\partial t} = -\nabla \cdot \mathbf{N}_{i,k} - \sum_h a_{1,k} s_{i,k,h} \frac{i_{h,1-k}}{n_h F} + \sum_l s_{i,k,l} \sum_{p \neq k} a_{k,p} r_{l,k-p} + \sum_g s_{i,k,g} \varepsilon_k R_{g,k} \tag{33}$$

In the above expression, ε_k is the volume fraction of phase k, $c_{i,k}$ is the concentration of species i in phase k, and $s_{i,k,l}$ is the stoichiometric coefficient of species i in phase k participating in heterogeneous reaction l, $a_{k,p}$ is the specific surface area (surface area per unit total volume) of the interface between phases k and p, $i_{h,l-k}$ is the normal interfacial current transferred per unit interfacial area across the interface between the electronically conducting phase and phase k due to electron-transfer reaction h and is positive in the anodic direction.

The term on the left side of the equation is the accumulation term, which accounts for the change in the total amount of species i held in phase k within a differential control volume over time. The first term on the right side of the equation keeps track of the material that enters or leaves the control volume by mass transport as discussed in later sections. The remaining three terms account for material that is gained or lost (i.e., source terms, S_ψ, in Equation (32)). The first summation includes all electron-transfer reactions that occur at the interface between phase k and the electronically conducting phase l; the second summation accounts for all other interfacial processes that do not include electron transfer like evaporation or condensation; and the final term accounts for homogeneous chemical reactions in phase k. It should be noted that in terms of an equation count, for n species there are only $n-1$ conservation equations needed, as one can be replaced by the sum of the other ones or, similarly, by the fact that the sum of the mole fractions equals 1:

$$\sum_i x_i = 1 \tag{34}$$

In the above material balance (Equation (33)), one needs an expression for the flux or transport of material. Often, this expression stems from considering only the interactions of the various species with the solvent

$$\mathbf{N}_{i,k} = -D_i \nabla c_{i,k} + c_i \mathbf{v}_k \tag{35}$$

where $\mathbf{v}_k$ is the mass-averaged velocity of phase k

$$\mathbf{v}_k = \frac{\sum_{i \neq s} M_i \mathbf{N}_{i,k}}{\rho_k} \tag{36}$$

One can see that if convection is neglected, Equation (35) results in Fick's law. Substitution of Equation (35) into Equation (33) results in the equation for convective diffusion, which, in terms of mass, is

$$\frac{\partial(\varepsilon_k \rho_k w_i)}{\partial t} + \nabla \cdot (\mathbf{v}_k \rho_k w_i) = \nabla \cdot \left(\rho_k D_i^{\text{eff}} \nabla w_i\right) + S_i \tag{37}$$

which is often used in computational-fluid-dynamic simulations. In the above expression, the reaction source terms are not shown explicitly, w_i is the mass fraction of species i, and the superscript ''eff'' is used to denote an effective diffusion coefficient due to different phenomena or phases as discussed later in this chapter.If the interactions among the various species are important, then Equation (35) needs to be replaced with the multicomponent Stefan–Maxwell equations that account for binary interactions among the various species

$$\nabla x_{i,k} = -\frac{x_{i,k}}{RT}\left(\overline{V}_i - \frac{M_i}{\rho_k}\right)\nabla p_k + \sum_{j \neq i} \frac{x_{i,k}\mathbf{N}_{j,k} - x_{j,k}\mathbf{N}_{i,k}}{\varepsilon_k c_{\text{T},k} D_{i,j}^{\text{eff}}} \tag{38}$$

where x_i and M_i are the mole fraction and molar mass of species i, respectively; $D_{i,j}^{\text{eff}}$ is the effective binary diffusion coefficient between species i and j; and $c_{\text{T},k}$ is the total concentration of species in phase k as derived from the ideal-gas law (Equation (14)). The first term on the right side accounts for pressure diffusion (e.g., in centrifugation) which often can be ignored, but on the anode side, the differences between the molar masses of hydrogen and water mean that it can become important in certain circumstances (Weber and Newman, 2005b). The second term on the right side stems from the binary collisions between various components. For a multicomponent system, Equation (38) results in the correct number of transport properties that must be specified to characterize the system, $1/2n(n-1)$, where n is the number of components and the $1/2$ is because $D_{i,j}^{\text{eff}} = D_{j,i}^{\text{eff}}$ by the Onsager reciprocal relationships.

The form of Equation (38) is essentially an inverted form of the type of Equation (35), as one is not writing the flux in terms of a material gradient but the material gradient in terms of the flux. This is not a problem, if one is solving the equations as written; however, many numerical packages require a second-order differential equation (e.g., see Equation (37)). To

do this with the Stefan–Maxwell equations, inversion of them is required. For a two-component system where the pressure diffusion is negligible, one gets Equation (35). For higher numbers of components, the inversion becomes cumbersome and analytic expressions are harder to obtain, resulting oftentimes in numerical inversion. In addition, the inversion results in diffusion coefficients that are more composition dependent. For example, Bird *et al*. (1960) show the form for a three-component system.

2.3.2 Charge

The conservation equation for charged species is an extension of the conservation of mass. Taking Equation (33) and multiplying by $z_i F$ and summing over all species and phases while noting that all reactions are charge balanced yield

$$\frac{\partial}{\partial t} F \sum_k \sum_i z_i c_{i,k} = -\nabla \cdot F \sum_k \sum_i z_i \mathbf{N}_{i,k} \tag{39}$$

where the charge and current densities can be defined by

$$\rho_e = F \sum_k \sum_i z_i c_{i,k} \tag{40}$$

and

$$\mathbf{i}_k = F \sum_i z_i \mathbf{N}_{i,k} \tag{41}$$

respectively. Because a large electrical force is required to separate charge over an appreciable distance, a volume element in the electrode will, to a good approximation, be electrically neutral; thus one can assume electroneutrality for each phase

$$\sum_i z_i c_{i,k} = 0 \tag{42}$$

The assumption of electroneutrality implies that the diffuse double layer, where there is significant charge separation, is small compared to the volume of the domain, which is normally (but not necessarily always) the case. The general charge balance (Equation (39)) assuming electroneutrality and the current definition (Equation (41)) becomes

$$\sum_k \nabla \cdot \mathbf{i}_k = 0 \tag{43}$$

While this relationship applies for almost all of the modeling, there are cases where electroneutrality does not strictly hold, including for some transients and impedance measurements, where there is charging and discharging of the double layer, as well as simulations at length scales within the double layer (typically on the order of nanometers). For these cases, the correct governing charge conservation results in Poisson's equation,

$$\nabla^2\Phi = \frac{\rho_e}{\varepsilon_0} \tag{44}$$

where ε_0 is the permittivity of the medium. For the diffuse part of the double layer, often a Boltzmann distribution is used for the concentration of species i

$$c_i = c_{i,\infty} \exp\left(-\frac{z_i F\Phi}{RT}\right) \tag{45}$$

To charge this double layer, one can derive various expressions for the double-layer capacitance depending on the adsorption type, ionic charges, etc. (Newman and Thomas-Alyea, 2004), where the double-layer capacitance is defined as

$$C_d = \left(\frac{\partial q}{\partial \Phi}\right)_{\mu_i, T} \tag{46}$$

where q is the charge in the double layer and the differential is at constant composition and temperature. To charge the double layer, one can write an equation of the form

$$i = C_d \frac{\partial \Phi}{\partial t} \tag{47}$$

where the charging current will decay with time as the double layer becomes charged.

For the associated transport of charge, one can use either a dilute-solution or concentrated-solution approach. In general, the concentrated-solution approach is more rigorous but requires more knowledge of all the various interactions (similar to the material-transport-equation discussion above). For the dilute-solution approach, one can use the Nernst–Planck equation,

$$\mathbf{N}_{i,k} = -z_i u_i F c_{i,k} \nabla \Phi_k - D_i \nabla c_{i,k} + c_{i,k} \mathbf{v}_k \tag{48}$$

where u_i is the mobility of species i. In the equation, the terms on the right side correspond to migration, diffusion, and convection, respectively. Multiplying Equation (48) by $z_i F$ and summing over the species i in phase k,

$$F \sum_i z_i \mathbf{N}_{i,k} = -F^2 \sum_i z_i^2 u_i c_{i,k} \nabla \Phi_k - F \sum_i z_i D_i \nabla c_{i,k} + F \sum_i z_i c_{i,k} \mathbf{v}_k \tag{49}$$

and noting that the last term is zero due to electroneutrality (convection of a neutral solution cannot move charge) and using the definition of current density (Equation (41)), one gets

$$\mathbf{i}_k = -\kappa_k \nabla \Phi_k - F \sum_i z_i D_i \nabla c_{i,k} \tag{50}$$

where κ_k is the conductivity of the solution of phase k

$$\kappa_k = F^2 \sum_i z_i^2 c_{i,k} u_i \tag{51}$$

When there are no concentration variations in the solution, Equation (50) reduces to Ohm's law,

$$\mathbf{i}_k = -\kappa_k \nabla \Phi_k \tag{52}$$

This dilute-solution approach does not account for interaction between the solute molecules which could be dominant for cases of cation contamination, in AEMFCs, and phenomena such as electroosmotic flow. Also, this approach will either use too many or too few transport coefficients depending on if the Nernst–Einstein relationship is used to relate mobility and diffusivity,

$$D_i = RTu_i \tag{53}$$

which only rigorously applies at infinite dilution. Thus, the concentrated-solution theory approach is recommended; however, the Nernst–Planck equation can be used in cases where most of the transport properties are unknown or where the complex interactions and phenomena being investigated necessitate simpler equations (e.g., transport of protons and water along a single-charged pore in the membrane).

The concentrated-solution approach for charge utilizes the same underpinnings as that of the Stefan–Maxwell equation, which starts with the original equation of multicomponent transport (Pintauro and Bennion, 1984)

$$\mathbf{d}_i = c_i \nabla \mu_i = \sum_{j \neq i} K_{i,j} \left(\mathbf{v}_j - \mathbf{v}_i \right) \tag{54}$$

where $\mathbf{d}_i$ is the driving force per unit volume acting on species i and can be replaced by an electrochemical-potential gradient of species i, and $K_{i,j}$ are the frictional interaction parameters between species i and j. The above equation can be analyzed in terms of finding expressions for $K_{i,j}$'s, introducing the concentration scale including reference velocities and potential definition, or by inverting the equations and correlating the inverse friction factors to experimentally determined properties. Which route to take depends on the phenomena being studied (e.g., membrane, binary salt solution, etc.) (Newman and Thomas-Alyea, 2004) and will be examined later for the membrane. If one uses a diffusion coefficient to replace the drag coefficients,

$$K_{i,j} = \frac{RTc_i c_j}{c_{\mathrm{T}} \mathbf{D}_{i,j}} \tag{55}$$

where $\mathbf{D}_{i,j}$ is an interaction parameter between species i and j based on a thermodynamic driving force, then the multicomponent equations look very similar to the Stefan–Maxwell ones (Equation (38)). In addition, using the above definition for $K_{i,j}$ and assuming that species i is a minor component and that the total concentration, c_{T}, can be replaced by the

solvent concentration (species 0), then Equation (54) for species i in phase k becomes

$$\mathbf{N}_{i,k} = -\frac{\mathbf{D}_{i,0}}{RT} c_{i,k} \nabla \mu_{i,k} + c_{i,k} \mathbf{v}_0 \tag{56}$$

This equation is very similar to the Nernst–Planck Equation (48), except that the driving force is the thermodynamic electrochemical potential, which contains both the migration and diffusive terms.

2.3.3 Momentum

Due to the highly coupled nature of momentum conservation and transport, both are discussed below. Also, the momentum or volume conservation equation is highly coupled to the mass or continuity conservation equation (Equation (33)). Newton's second law governs the conservation of momentum and can be written in terms of the Navier–Stokes equation (Bird *et al.*, 2002)

$$\frac{\partial(\rho_k \mathbf{v}_k)}{\partial t} + \mathbf{v}_k \cdot \nabla(\rho_k \mathbf{v}_k) = -\nabla p_k + \mu_k \nabla^2 \mathbf{v}_k + S_{\mathrm{m}} \tag{57}$$

where μ_k and $\mathbf{v}_k$ are the viscosity and mass-averaged velocity of phase k, respectively. The transient term in the momentum conservation equation represents the accumulation of momentum with time and the second term describes convection of the momentum flux (which is often small for PEMFC designs). The first two terms on the right side represent the divergence of the stress tensor and the last term represents other sources of momentum, typically other body forces like gravity or magnetic forces. However, for PEMFCs, these forces are often ignored and unimportant, that is, S_{m}=0. It should be noted that for porous materials, as discussed below, the Navier–Stokes equations are not used and instead one uses the more empirical Darcy's law for the transport equation,

$$\mathbf{v}_k = -\frac{k_k}{\mu_k} \nabla p_k \tag{58}$$

This transport equation can be used as a first-order equation or combined with a material balance (Equation (33)) to yield

$$\frac{\partial(\rho_k \varepsilon_k)}{\partial t} = \nabla \cdot \left(-\rho_k \frac{k_k}{\mu_k} \nabla p_k \right) + S_{\mathrm{m}} \tag{59}$$

which is similar to including it as a dominant source term. In the above expression, k_k is the effective permeability of phase k. Since Darcy's law is first order and Navier–Stokes is second order, one losses a boundary condition which is the no-slip condition at the interior walls of the porous medium. There are extensions to Darcy's law that try and address this, but these approaches are beyond the scope of this chapter and the reader is referred to texts on this subject (Bear, 1988; Dullien, 1992).

2.3.4 Energy

Electrochemical reactions in a fuel cell release electrical energy and heat energy as discussed above. While electrical energy is accounted for by the flow of charge through the external circuit, the heat energy is conducted by the components and rejected either into cooling plates/channels or to the external environment. The heat causes an increase in the local temperature, which affects local properties such as diffusion coefficients, ionomer water content, etc., and may also result in different transport mechanisms (e.g., phase-change-induced flow of water). Throughout all layers of the PEMFC, the same transport and conservation equations exist for energy with the same general transport properties, and only the source terms vary. Therefore, these equations and properties are explored below and not really expanded upon in the rest of this chapter.

The conservation of thermal energy can be written as

$$\rho_k \hat{C}_{p_k}\left(\frac{\partial T_k}{\partial t} + \mathbf{v}_k \cdot \nabla T_k\right) + \left(\frac{\partial \ln \rho_k}{\partial \ln T_k}\right)_{p_k, x_{i,k}}\left(\frac{\partial p_k}{\partial t} + \mathbf{v}_k \cdot \nabla p_k\right) = Q_{k,p} - \nabla \cdot \mathbf{q}_k - \tau : \nabla \mathbf{v}_k + \sum_i \overline{H}_{i,k} \nabla \cdot \mathbf{J}_{i,k} - \sum_i \overline{H}_{i,k} \mathfrak{R}_{i,k} \tag{60}$$

In the above expression, the first term represents the accumulation and convective transport of enthalpy, where $\hat{C}_{p_k}$ is the heat capacity of phase k which is a combination of the various components of that phase. The second term is energy due to reversible work. For condensed phases, this term is negligible, and an order-of-magnitude analysis for ideal gases with the expected pressure drop in a PEMFC demonstrates that this term is negligible compared to the others. The first two terms on the right side of Equation (60) represent the net heat input by conduction and interphase transfer. The first is due to heat transfer between two phases

$$Q_{k,p} = h_{k,p} a_{k,p} \left(T_p - T_k\right) \tag{61}$$

where $h_{k,p}$ is the heat-transfer coefficient between phases k and p per interfacial area. Most often, this term is used as a boundary condition, as it occurs only at the edges. However, in some modeling domains (e.g., along the channel), it may need to be incorporated as above. The second term is due to the heat flux in phase k

$$\mathbf{q}_k = -\sum_i \overline{H}_{i,k} \mathbf{J}_{i,k} - k_{T_k}^{\text{eff}} \nabla T_k \tag{62}$$

where $\overline{H}_{i,k}$ is the partial molar enthalpy of species i in phase k, $\mathbf{J}_{i,k}$ is the flux density of species i relative to the mass-average velocity of phase k

$$\mathbf{J}_{i,k} = \mathbf{N}_{i,k} - c_{i,k} \mathbf{v}_k \tag{63}$$

and $k_{T_k}^{\text{eff}}$ is the effective thermal conductivity of phase k. The third term on the right side of Equation (60) represents viscous dissipation, the heat generated by viscous forces, where τ is the stress tensor. This term is also

small, and for most cases can be neglected. The fourth term on the right side comes from enthalpy changes due to diffusion. Finally, the last term represents the change in enthalpy due to reaction

$$\sum_i \overline{H}_{i,k}\Re_{i,k} = -\sum_h a_{1,k} i_{h,1-k}\left(\eta_{s_{h,1-k}} + \prod_h\right) - \sum_{p\neq k}\Delta H_l a_{k,p} r_{l,k-p} - \sum_g \Delta H_g R_{g,k} \tag{64}$$

where the expressions can be compared to those in the material conservation Equation (33). The above reaction terms include homogeneous reactions, interfacial reactions (e.g., evaporation), and interfacial electron-transfer reactions. As discussed above, the irreversible heat generation is represented by the activation overpotential and the reversible heat generation is represented by the Peltier coefficient, $\prod_h$ (see Figure 3 and Equation (18)). Upon comparison to Equations (18) and (10), the Peltier coefficient for charge-transfer reaction h can be expressed as

$$\prod_h \approx \frac{T}{n_h F}\sum_i s_{i,k,h}\overline{S}_{i,k} = T\frac{\Delta S_h}{n_h F} \tag{65}$$

where ΔS_h is the entropy of reaction h. The above equation neglects transported entropy (hence the approximate sign), and the summation includes all species that participate in the reaction (e.g., electrons, protons, oxygen, hydrogen, water). While the entropy of the half-reactions that occurs at the catalyst layers (Equations (1) and (2)) is not truly obtainable since it involves knowledge of the activity of an uncoupled proton, the Peltier coefficients have been measured experimentally for these reactions, with most of the reversible heat due to the four-electron ORR (Lampinen and Fomino, 1993; Shibata and Sumino, 1985).

It is often the case that because of the intimate contact between the gas, liquid, and solid phases within the small pores of the various PEMFC layers, that equilibrium can be assumed such that all of the phases have the same temperature as each other for a given point in the fuel cell. Doing this eliminates the phase dependences in the above equations and allows for a single thermal energy equation to be written. Neglecting those phenomena that are minor as mentioned above and summing over the phases results in

$$\begin{aligned}\sum_k \rho_k \hat{C}_{p_k}\frac{\partial T}{\partial t} = &-\sum_k \rho_k \hat{C}_{p_k}\mathbf{v}_k\cdot\nabla T + \nabla\cdot\left(k_T^{\text{eff}}\nabla T\right) + \sum_k \frac{\mathbf{i}_k\cdot\mathbf{i}_k}{\kappa_k^{\text{eff}}} \\ &+\sum_h i_h\left(\eta_h + \prod_h\right) - \sum_h \Delta H_h r_h\end{aligned} \tag{66}$$

where the expression for Joule or ohmic heating has been substituted from the third term in the right side of Equation (60)

$$-\sum_i \mathbf{J}_{i,k}\cdot\nabla\overline{H}_{i,k} = -\mathbf{i}_k\cdot\nabla\Phi_k = \frac{\mathbf{i}_k\cdot\mathbf{i}_k}{\kappa_k^{\text{eff}}} \tag{67}$$

In Equation (66), the first term on the right side is energy transport due to convection, the second is energy transport due to condition, the third is the ohmic heating, the fourth is the reaction heats, and the last represents reactions in the bulk which include such things as vaporization/condensation and freezing/melting. As noted above, heat lost to the surroundings (i.e., Equation (61)) is only accounted for at the boundaries of the cell. In terms of magnitude in a PEMFC, the major heat generation sources are the ORR and the water phase changes, and the main mode of heat transport is through conduction.

It should also be noted that the total heat generation is still given by Equation (9) upon summation over all the charge-transfer reactions

$$Q = \sum_{k-p}\sum_h a_{k,p} i_{h,k-p}(U_{H_h} - V) \tag{68}$$

This equation can be used if one only cares about the total heat generation and not its distribution (i.e., assuming that the inside domains are isothermal).

The assumption of local thermal equilibrium also means that an overall effective thermal conductivity is needed, because there is only a single energy equation. One way to calculate this thermal conductivity is to use Bruggeman factors (Bruggeman, 1935),

$$k_T^{\text{eff}} = \sum_k \varepsilon_k^{1.5} k_{T_k} \tag{69}$$

Another method is to average the thermal conductivity in terms of resistances (Berning *et al.*, 2002; Mazumder and Cole, 2003),

$$k_T^{\text{eff}} = -2k_{\text{s}} + \frac{1}{\frac{\varepsilon_{\text{o}}}{2k_{\text{s}}+k_{\text{G}}} + \frac{1-\varepsilon_{\text{o}}}{3k_{\text{G}}}} \tag{70}$$

where ε_{o} is the porosity of the domain and k_{s} and k_{G} represent the thermal conductivity of the solids (including liquid) and gas phases, respectively. A final way to calculate an effective thermal conductivity is to realize that the thermal conductivity of the solid is the larger and use that value, although the porosity and tortuosity should be considered for the different solid phases.

3. MODELING ASPECTS OF FUEL CELLS

In this section, the focus is on the specific transport equations for each domain or type. Included are the approaches taken for modeling and simulating the domain, and deviations from the general equations

presented above are noted. In addition, some extensions are discussed that include analysis and modeling of specific phenomena and current topics of interest in PEMFC modeling.

3.1 Membrane

The polymer electrolyte that forms the core of a PEFC conducts ions between the catalyst layers, while inhibiting crossover of reactants. Though there are various types of membranes that have been studied for PEMFCs, due to its desirable properties, Nafion® and its class of ionomers are the most experimented, modeled, and used membranes. Nafion is a random copolymer of hydrophobic polytetrafluoroethylene with side chains of hydrophilic polysulfonyl fluoride vinyl ether as shown in Figure 6a and is termed a perfluorinated sulfonic-acid (PFSA) ionomer. The anionic sulfonic-acid sites are attached to the side chain, and hence the concentration of cations (i.e., protons), within the membrane, is fixed as long as there are no ionic contaminants. The structure of Nafion as shown schematically in Figure 6b is a phase-separated structure with hydrophilic or water-filled domains that include the sulfonic-acid sites surrounded by hydrophobic backbone and crystallites. The transport of all of the relevant species occurs within the hydrophilic domains, and as such, the transport properties are highly dependent on the water content of the membrane as discussed later.

A good model of the membrane must contain certain key elements. Foremost among these is that it must be based on and agree with the physical reality and phenomena that have been observed with these membranes. Further, expressions for the various properties of the membrane should have the relevant dependences such as on temperature and water content. These property expressions can be found by everything from empirical relations to detailed molecular modeling. At its simplest, a membrane model should predict the water flux and the potential drop through the membrane. The potential drop is necessary in calculating polarization effects and the water flux directly impacts the water management of the PEFC, which is one of the most significant components of fuel-cell performance. In terms of fluxes, a model should describe the three main fluxes in the membrane as shown in Figure 7.

The three main fluxes through the membrane are a proton flux that goes from anode to cathode, a water electroosmotic flux that develops along with the proton flux and a water-gradient flux. This last flux is sometimes known as the water back flux or back-diffusion flux and, as discussed below, has various interpretations including diffusion and convection. The protons move via hopping across the hydrogen-bond network linked by the sulfonic-acid sites or transferred by a vehicle

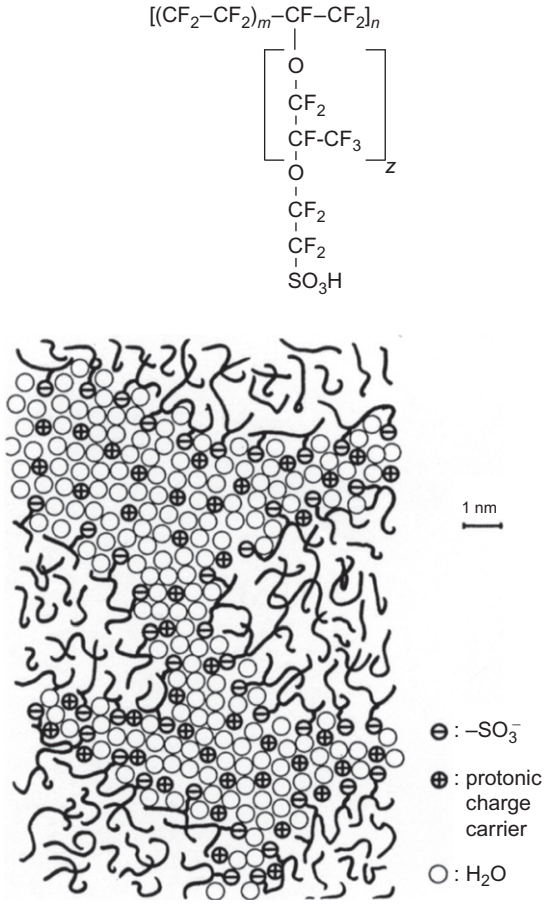

Figure 6 Schematic of the (a) chemical formula, where *m* is between 6 and 13 and *z* is 3, and (b) structure of Nafion (Kreuer *et al.*, 2004).

mechanism of hydrated water/proton clusters (e.g., hydronium, Zundel, or Eigen ions). These various fluxes have been simulated with a whole range of models, from the atomistic and molecular through to the macroscopic. The microscopic models are specific to the type of membrane and try to predict the membrane microstructure and phase separation due to water uptake, as well as examine transport through it at a fundamental level, including effects such as pore-level ion transport. The macroscopic models are often more empirical and focus on describing transport and the change of properties in a homogenous domain considering a few basic properties of the polymer membrane. As the membrane domain is treated as homogeneous, the macroscopic modeling approach may be applicable

for different types of membranes in a macrohomogeneous fashion. As per the overall approach of this chapter, discussion is made on the macroscopic models; for microscopic analyses, there are various reviews including that of Kreuer *et al*. (2004).

3.1.1 Governing equations

As described above, the material and current conservation Equations ((33) and (43), respectively) holds good. As there are no reactions within the membrane, at steady state, the current and species fluxes are constant. While in principal one can use dilute−solution theory to describe ion transport, this is not advisable for the membrane because it neglects electroosmosis and concentrated−solution theory can readily implemented. In addition, temperature is handled through Equation (66) in the membrane, where Joule heating is the only heat source and conduction is the only method of heat transfer.

From Equation (54), the multicomponent equations for water and protons can be written for the three-component membrane, water, and proton system

$$\begin{aligned} c_+\nabla\mu_+ &= K_{\mathrm{w},+}(\mathbf{v}_\mathrm{w}-\mathbf{v}_+)+K_{\mathrm{m},+}(-\mathbf{v}_+) \\ c_\mathrm{w}\nabla\mu_\mathrm{w} &= K_{\mathrm{w},+}(\mathbf{v}_+-\mathbf{v}_\mathrm{w})+K_{\mathrm{m,w}}(-\mathbf{v}_\mathrm{w}) \end{aligned} \tag{71}$$

where the subscripts +, w, and m signify the protons, water, and membrane, respectively. In writing the above equations, the membrane velocity (stationary) is taken as the reference velocity. To use the above equations, the frictional coefficients must be related to measurable quantities. For the three-component system, there needs to be three independent transport properties. The equations can be inverted to

$$\mathbf{N}_+ = c_+\mathbf{v}_+ = -L_{+,+}c_+^2\nabla\mu_+ - L_{+,\mathrm{w}}c_+c_\mathrm{w}\nabla\mu_\mathrm{w} \tag{72}$$

and

$$\mathbf{N}_\mathrm{w} = c_\mathrm{w}\mathbf{v}_\mathrm{w} = -L_{\mathrm{w},+}c_+c_\mathrm{w}\nabla\mu_+ - L_{\mathrm{w,w}}c_\mathrm{w}^2\nabla\mu_\mathrm{w} \tag{73}$$

where the $L_{i,j}$'s ($=L_{j,i}$) are related directly to the $K_{i,j}$'s (Fuller, 1992). The $L_{i,j}$'s can also be related to experimentally measured transport properties

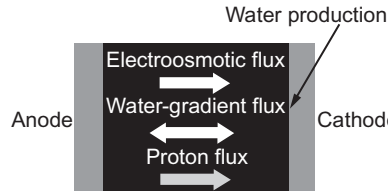

Figure 7 Schematic of a proton-exchange membrane showing the various dominant fluxes through it.

using the following set of three orthogonal experiments (Pintauro and Bennion, 1984).

As the membrane contains only protons as charge carriers (the transference number of protons is 1 for this system), the current density in the membrane phase (subscript 2) is by Equation (41)

$$\mathbf{i}_2 = Fz_+\mathbf{N}_+ = F\mathbf{N}_+ \tag{74}$$

Also, the potential in the membrane can be defined by

$$\Phi_2 = \frac{\mu_+}{F} \tag{75}$$

For the first of the three orthogonal experiments, one considers the case where $\nabla\mu_w$=0, and the conductivity of the membrane is measured. From Equation (72) using Equation (75) and Ohm's law (Equation (52)), the following can be deduced

$$L_{+,+} = \frac{\kappa}{F^2c_+^2} \tag{76}$$

For the next experiment, consider the case where again $\nabla\mu_w$=0, but now a small current is passed through the membrane and the flux of water through the membrane is measured. Using Equation (72) with Equation (74) and the definition of the electroosmotic coefficient or transport number of water: the number of water molecules is carried across the membrane by each hydrogen ion in the absence of a water concentration gradient,

$$\xi = \frac{\mathbf{N}_w}{\mathbf{N}_+} \tag{77}$$

yields the relation

$$L_{w,+} = \frac{\kappa\xi}{F^2c_+c_w} \tag{78}$$

Finally, consider the case where there is no current, but water flows due to its chemical-potential gradient. Using the above equations and the relation

$$\mathbf{N}_w = -\alpha\nabla\mu_w \tag{79}$$

where α is called the transport coefficient, Equations (72) and (74) give

$$L_{w,w} = \frac{1}{c_w^2}\left[\alpha + \frac{\kappa\xi^2}{F^2}\right] \tag{80}$$

In terms of the above three properties, Equations (72) and (73) become

$$\mathbf{i}_2 = -\kappa\nabla\Phi_2 - \frac{\kappa\xi}{F}\nabla\mu_w \tag{81}$$

and

$$\mathbf{N}_w = -\frac{\kappa\xi}{F}\nabla\Phi_2 - \left(\alpha + \frac{\kappa\xi^2}{F^2}\right)\nabla\mu_w \tag{82}$$

respectively. These two equations combined with the material and charge balances and energy equation constitute a closed set of independent equations that completely describe the transport within the membrane for a concentrated-solution system composed of water, proton, and membrane. The boundary conditions used in conjunction with the above equations can vary and are to some degree simulation dependent. Normally, the current density, water flux, reference potential, and water chemical potential are specified, but two water chemical potentials or the potential drop in the membrane can also be used. If modeling more regions than just a membrane, additional mass balances and internal boundary conditions must be specified. It should be noted that in the derivation above nothing has been stated about the mode of transport; thus, the equations above are general.

There are thought to be two main mechanisms of water transport within the membrane, that driven by concentration and that driven by a hydraulic pressure. As noted above, Equations (81) and (82) utilize a chemical-potential driving force. This driving force can be related to either concentration (activity) or pressure by the definition of chemical potential

$$\nabla \mu_{\mathrm{w}} = RT \nabla \ln a_{\mathrm{w}} + \overline{V}_{\mathrm{w}} \nabla p \tag{83}$$

where a_{w} is the activity of water in the membrane. Therefore, the above expressions take into account both mechanisms using the single, thermodynamic driving force as discussed in more detail below.

Reactant gases can also transport through the membrane, thus decreasing the cell potential and resulting in possible durability and safety concerns. Gas crossover limits the minimum thickness of the membrane. To model the crossover, one can use the expression

$$\mathbf{N}_i = -\psi_i \nabla p_i \tag{84}$$

where ψ_i and p_i are the permeation coefficient and partial pressure of species i, respectively. This approach is valid as the crossover gases are very dilute. The permeation coefficient is used as it allows for a single variable to describe the transport, instead of two (i.e., diffusion and solubility coefficients), each with their dependences on temperature, etc., which may even offset each other. The above equation requires a simple boundary condition of continuous partial pressure of the gas at the membrane interface. To be rigorous, one should add a convective term to Equation (84) as is done in Equation (37); however, this convective term now signifies the amount of gas carried with the net water flux in the membrane, and a back-of-the-envelope calculation shows that such a convective flow is at least an order of magnitude less than the permeation one, and thus it can be disregarded to a first approximation. The permeation coefficients, like the other transport properties, are

expected to depend mainly on the membrane water content and temperature.

3.1.2 Water content and transport properties

As noted above, all the transport properties are a function of the water content of the membrane, which itself is a function of the environmental conditions. The water content is characterized by the variable λ, which is the moles of water per mol of sulfonic-acid sites. To understand how this quantity varies, one can examine a water-uptake curve as shown in Figure 8. As is seen, the water uptake increases slightly due to primary solvation of the sulfonic-acid sites and then increases almost exponentially due to the formation of bulk-like water within the hydrophilic domains. Also shown is that there is a difference of water content between liquid water and fully saturated vapor (i.e., water activity is the same), which is known as Schroeder's paradox, and is due to interfacial realignment of the membrane depending on which phase it is in contact with. The magnitude of the uptake is also dependent on such issues as the membrane chemistry and possible mechanical reinforcement, thermal history, etc.

There are numerous ways that one can and people have modeled the water-uptake isotherm. The approaches range from fitting the curve with a polynomial expression to modeling it more rigorously using a balance between solvation and backbone mechanical energies. Modeling has also been done on various length scales as well for the water uptake. Unfortunately, there is no true consensus on the model to be used for water uptake, and a review and discussion of such models is beyond the scope of this chapter. Herein, it is assumed that one has the uptake isotherm (i.e., Figure 8) either experimentally or theoretically that one can use to determine the membrane's water content.

The water-uptake isotherm is an equilibrium property of the membrane. However, during operation, it is believed that there may be an interfacial resistance that effectively changes the water content of the membrane (He *et al.*, 2011; Zhao *et al.*, 2011). This resistance is humidity dependent and can be a substantial component of the total membrane resistance toward transport, especially for thin membranes or at low water contents (i.e., dry environments). To account for this effect, the membrane water-uptake boundary condition is altered to include a mass-transfer coefficient instead of assuming equilibrium (i.e., using Figure 8 directly)

$$N = k_{\mathrm{mt}}(a_{\mathrm{in}} - a_{\mathrm{out}}) \tag{85}$$

where in and out refer to the water activities directly inside and outside of the membrane interface and k_{mt} is a mass-transfer coefficient. This approach is the same as including a surface reaction (e.g., condensation)

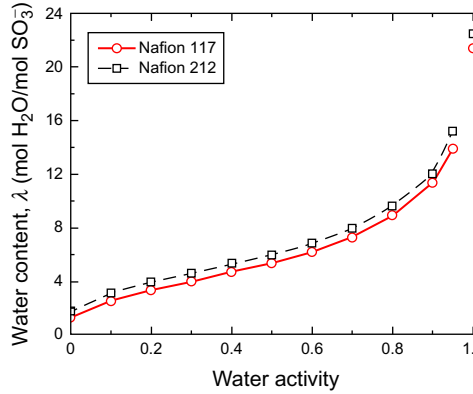

Figure 8 Water-uptake curve of Nafion 117 as measured by dynamic-vapor sorption.

at the membrane interface. Finally, since the water is in a condensed state within the membrane, water uptake should involve the release or consumption of phase-change heat, which should be accounted for in the energy conservation Equation (66).With the dramatic increase in water content, one can assume that the membrane swells. This swelling will change the dimensions of the membrane, thus affecting the gradients in the governing equations. Membrane swelling can be either isotropic or anisotropic and depends strongly on if and how the membrane is mechanically reinforced or if it has substantial crosslinking. In any case, analysis of membranes' mechanical properties and force balances demonstrates that the membrane will swell as the compressive load of a typical cell assembly is not significant enough to compress it (Kusoglu *et al.*, 2011). To account for swelling, one can use a variable transformation such that

$$z' = \frac{z}{1 + s\frac{\overline{V}_w}{\overline{V}_m}\lambda} \tag{86}$$

where z is a given spatial dimension, s is the swelling factor in dimension z, and $\overline{V}_m$ is the partial molar volume of the dry membrane

$$\overline{V}_m = \frac{EW}{\rho_{m,o}} \tag{87}$$

where $\rho_{m,o}$ is the density of the dry membrane and EW is the membrane's equivalent weight. Similarly, one can calculate the swelling dimensional change based on the average water content of the membrane, $\hat{\lambda}$, using an expression of the form of Equation (86). However, since $\hat{\lambda}$ is not known *a priori*, one must iterate over the entire simulation until the value converges or one can use the following set of differential equations to

calculate it during the simulation. The first equation is an expression of the average water content as an integral

$$\hat{\lambda} = \frac{1}{l}\int_0^{z=l} \lambda(z)\mathrm{d}z = \int_0^1 \lambda(\varsigma)\mathrm{d}\varsigma \tag{88}$$

where the equation has been nondimensionalized. The second equation arises from the thickness being a scalar quantity that is uniform

$$\frac{\mathrm{d}l}{\mathrm{d}\varsigma} = 0 \tag{89}$$

These two equations are solved with the swelling boundary condition given by Equation (86) and applied at ς=1. The above accounts for the dimensional changes; however, the impact on the transport properties also needs to be considered. As the membrane swells, its volume increases

$$V = \overline{V}_{\mathrm{m}} + \lambda \overline{V}_{\mathrm{w}} \tag{90}$$

which can affect the transport properties.

As noted in the previous section, there are three main transport properties within the membrane: conductivity, electroosmotic coefficient, and transport coefficient. All have been experimentally measured and are functions of temperature and water content (λ) for a given membrane. The first two are relatively straightforward to interpret and use. The transport coefficient requires some further discussion. As discussed above, the chemical potential gradient can be seen as being composed of an activity and a pressure component. For a vapor-equilibrated membrane, the impact of pressure is expected to be negligible, while for a liquid-equilibrated membrane, the activity of water is expected to be constant. Thus, for each isolated case, one can derive the expected expression for the transport coefficient. For a pressure-driven process, the measured variable is the permeability (see Darcy's law, Equation (58)) and thus

$$\alpha_{\mathrm{L}} = \frac{k_{\mathrm{sat}}}{\mu \overline{V}_{\mathrm{w}}^2} \tag{91}$$

where the subscript L denotes that it is from a liquid-equilibrated measurement, μ is the viscosity, and k_{sat} is the membrane permeability. For an activity-driven process, the diffusivity is the measured parameters and thus

$$\alpha_{\mathrm{V}} = \mathbf{D}_{\mathrm{w}} \frac{c_{\mathrm{w}}(\lambda+1)}{RT} \tag{92}$$

where c_{w} is the concentration of water in the membrane (assuming swelling),

$$c_{\mathrm{w}} = \frac{\lambda}{\overline{V}_{\mathrm{w}}\lambda + \overline{V}_{\mathrm{m}}} \tag{93}$$

If the membrane is partially liquid and vapor equilibrated, then the two α values must be averaged in some fashion. Typically, the α_L is much larger than α_V, and it is thought that during operation when there is liquid water, α_L dominates and is appropriate to use (Adachi *et al.*, 2009). This is also in agreement with measurements that say that diffusion is relatively fast within the membrane and is limited by interfacial mass transfer as discussed above. For a vapor-equilibrated membrane, α_V (Equation (92)) can be used in Equation (82) to result in an expression that is similar to the standard diffusion equation. However, the diffusion coefficient used, $\mathbf{D}_w$, is based on a thermodynamic driving force. While this is valid for interpretation from NMR measurements, it can be correlated to the Fickian diffusion coefficient by

$$D_w = \frac{\partial \ln a_w}{\partial \ln c_w} \mathbf{D}_w \tag{94}$$

which essentially takes into account the change in water activity coefficient upon uptake. This expression can easily be calculated from the water-uptake isotherm (Figure 8). It should also be noted that this diffusivity is for steady-state transport, and for dynamic transport, a different and lower diffusion coefficient is determined due to the simultaneous occurrence of both water transport and sorption.

3.1.3 Multi-ion transport

The analysis and discussion above is centered on having the proton being the only mobile ion inside the membrane. There are instances where this is not the case, for example, that of cation contamination including Pt ions due to Pt dissolution, flowfield corrosion products, salts from the environment, etc. These ions will ion-exchange with the protons in the membrane and can cause dramatic decreases in cell performance. In addition, the issue of multi-ion transport in the membrane is especially critical in AEMFCs, where carbon dioxide from the air will cause a competition between the hydroxide ions and the bicarbonate ions in the membrane.

To calculate the distribution of ions in the membrane in contact with a reservoir, one needs to consider chemical equilibrium among the various species in the membrane and their counterparts in the external reservoir. To do this, one needs to calculate the concentration distribution of each ion inside the pore. This distribution can be written as a modified Boltzmann distribution (see Equation (45))

$$c_i(r) = c_i^{ext} \exp\left(-\frac{z_i F \Phi(r)}{RT} - \frac{A_i}{RT}\left(\frac{1}{\varepsilon_r(r)} - \frac{1}{\varepsilon_r^{ext}} \right) \right) \tag{95}$$

where r is the radial position of the pore, ext denotes the external reservoir, A_i is an ion hydration constant of species i (see Bontha and Pintauro, 1994 for values), and ε_r is the dielectric of the medium. In the above expression, the

first term represents electrostatic attraction/repulsions of ions and the second relates the effects of a changing dielectric medium. If the dielectric is constant and the same as the reservoir, then the expression becomes a normal Boltzmann distribution.

To calculate the distribution, the dielectric constant and potential distributions must be known. The dielectric-constant distribution can be determined using Booth's equation (Booth, 1951)

$$\varepsilon(r) = n^2 + \frac{3\left(\varepsilon_r^{\text{ext}} - n^2\right)}{\zeta\nabla\Phi(r)}\left[\coth(\zeta\nabla\Phi(r)) - \frac{1}{\zeta\nabla\Phi(r)}\right] \tag{96}$$

where n is the refractive index of the solution and ζ is

$$\zeta = \left(\frac{5\eta}{2k_{\text{B}}T}\right)\left(n^2 + 2\right) \tag{97}$$

where k_{B} is Boltzmann's constant and η is the dipole moment of the solvent molecule. Finally, the potential distribution can be calculated by solving Poisson's Equation (44). Solving Equations (95), (96), and (44) simultaneously yields the concentration distributions of the various ions and the potential distribution within the pore.

The results of the partition calculations demonstrate an order of magnitude larger dielectric constant near the pore walls where the sulfonic-acid sites reside than in the pore middle (Kreuer *et al.*, 2004; Pintauro and Verbrugge, 1989). In fact, the change of the dielectric constant can be correlated to the existence of bulk-like water. The above approach allows the prediction of ion partitioning by the fuel-cell membranes. For the AEMFC, one must also consider the equilibrium between carbon dioxide and its carbonate forms.

The above analysis yields distributions of the potential and ions but does not treat their transport. As discussed above, Nernst–Planck Equations (48) can be used for the transport along with the multi-ion definitions of current density (Equation (41)) and conductivity (Equation (51)), the modified Ohm's law (Equation (50)), and electroneutrality (Equation (34)). Due to the presence of more species, more properties are required. These can take the form of the conductivity, and species' mobilities, diffusion coefficients, and transference numbers

$$t_j = \frac{z_j^2 u_j c_j}{\sum_i z_i^2 u_i c_i} \tag{98}$$

which is the fraction of current carried by the ion j in the absence of concentration gradients. Without other ions, this value is 1 for protons, and it can be used as an indication of the current-transport efficiency. Also, the electroosmotic coefficient is basically the transference number of water (see Equation (77)).

However, for these multicomponent systems, concentrated-solution theory is more appropriate as it contains the correct number of transport properties, and also the binary ion/ion interactions are expected to be important. The downside is that the analysis is much more complex and requires more knowledge of the various transport properties and activity coefficients. For this analysis, equations of the form of Equation (54) can be used along with the definitions and electroneutrality. For example, for a four-component system composed of protons (H^+), single-charged cations (X^+), water (w), and membrane (M^-), Equation (54) can be written as

$$\nabla\mu_{X^+} = RT\left(\frac{\nabla x_{X^+}}{x_{X^+}} - \frac{\nabla x_{H^+}}{x_{H^+}}\right) + b\left(\nabla\left(y_{HM}^2\right) - \nabla\left(y_{KM}^2\right)\right) + F\nabla\Phi_2 \tag{99}$$

$$\nabla\mu_{M^-} = RT\left(\frac{\nabla x_{H^+}}{x_{H^+}} + \frac{\nabla x_{M^-}}{x_{M^-}}\right) + b\nabla\left(y_{XM}^2\right) - F\nabla\Phi_2 \tag{100}$$

and

$$\nabla\mu_w = RT\frac{\nabla x_w}{x_w} \tag{101}$$

where the potential was defined relative to the hydrogen potential as before (see Equation (75)), y_i is the mole fraction of cation i relative to the total number of cations, and b is a constant related to the activity coefficient. These equations can be solved along with the concentration-dependent water-uptake isotherm, diffusivities, and activity coefficients and the equations discussed above. Similarly, for the AEMFC, the above analysis can hold except with anions instead of cations.

To understand some of the impacts, Figure 9 shows the simulation results for potassium ions contaminating Nafion. The calculated limiting current density is due to the proton concentration becoming zero at the cathode catalyst layer and is the maximum current density that can be sustained through the membrane. From the figure, at low to medium cation contaminant concentration, there is not a substantial impact on performance, especially for thinner membranes. However, as the average concentration of K^+ increases, this effect becomes limiting in the cell.

3.2 Porous media

The porous media within a PEMFC (Figure 1) include the catalyst layers and the diffusion media, which are often composed of multiple layers including gas-diffusion and microporous layers. Figure 10 shows scanning-electron micrographs of some of the PEMFC porous media, where the catalyst layer has much smaller pores and is more isotropic than the fibrous gas-diffusion layer. The diffusion media play the important roles of mechanical support and spreading the reactant gas and electrons over the electrode while removing the product water out of the electrode to

the gas channel. As these two processes are counteracting processes, a balance is to be achieved for a maximum utilization of electrode catalyst while minimizing the mass-transport losses. As seen in the polarization curve (Figure 2), the mass-transfer limitation posed by the cathodic processes significantly reduces efficiency, especially at high current densities where water production is greatest. Any improvement in utilizable power density could significantly decrease the electrode area required for getting the same power, thereby reducing cost. As discussed above, some of the water generated at the cathode also back diffuses to the anode. As the diffusion of hydrogen in water is faster than that of oxygen, the mass-transport loss at the anode due to water accumulation in the anode side is often negligible and ignored. The key aspect of the porous media within the PEMFC is understanding multiphase (vapor and liquid) flow and controlling the water management.

In terms of modeling, the energy conservation Equation (66) holds with conduction being the dominant energy transfer mechanism, with the heat leaving the system through contact with the flowfield ribs, which also results in some preferential condensation at those spots, especially since water has to diffuse laterally to leave the layer from there. In terms of electron transport, Ohm's law is used for the electronic phase (1)

$$\mathbf{i}_1 = -\sigma_o \varepsilon_1^{1.5} \nabla \Phi_1 \tag{102}$$

where, ε_1 and σ_o are the volume fraction and electrical conductivity of the electronically conducting phase 1, respectively. The above equation has been adjusted for porosity and tortuosity using a Bruggeman correlation. In the diffusion media, carbon is the conducting phase and the other solid component, Teflon®, is insulating.

Generally, due to the low operating temperature and pressure, the gas phase is assumed to be ideal and follow the ideal-gas law (Equation (14)). As discussed above, although a dilute-solution approach using the convective-diffusion Equation (37) can be used, it is more appropriate to use the Stefan–Maxwell Equations (38) for the transport equations. In terms of diffusion, both gas–gas interactions and gas–solid interactions are expected to occur. These later ones can be related to diffusion coefficient or interaction parameter between the gas species and the wall. If one takes the wall to be a species (and uses that as the reference velocity frame), then one can derive a consistent expressions of the form

$$\nabla x_i = \sum_{j \neq i} \frac{x_i \mathbf{N}_j - x_j \mathbf{N}_i}{c_T D_{i,j}^{\text{eff}}} - \frac{\mathbf{N}_i}{c_T D_{K_i}^{\text{eff}}} \tag{103}$$

where G denotes the gas phase and the effect of tortuosity and porosity on the diffusion coefficients is addressed by

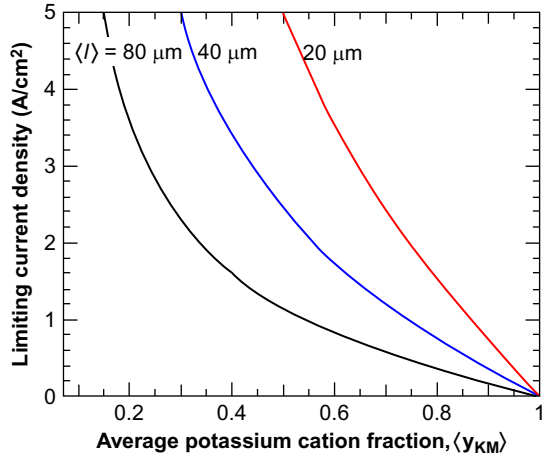

Figure 9 Limiting current density as a function of the average relative fraction of potassium cations and average swollen membrane thickness for a 1100 equiv. weight membrane.

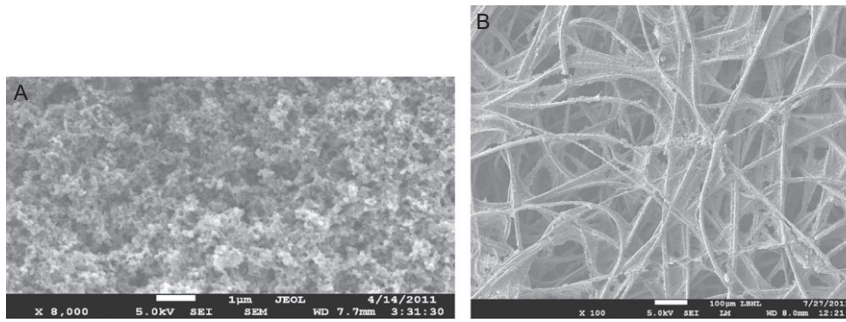

Figure 10 Scanning-electron micrographs of a typical (a) catalyst layer and (b) carbon paper gas-diffusion layer; note the two-order-of magnitude difference in the magnification (1 and 100 micrometer, respectively).

$$D_{i,j}^{\text{eff}} = \frac{\varepsilon_{\text{G}}}{\tau_{\text{G}}} D_{i,j} \tag{104}$$

where τ_{G} is the tortuosity or diffusional path length to be traveled to cross a region of certain thickness, and which is often calculated by a Bruggeman factor,

$$\tau_{\text{G}} = \varepsilon_{\text{G}}^{-0.5} \tag{105}$$

but this is believed to underpredict the effect. In Equation (103), $D_{K_i}^{\text{eff}}$ represents the Knudsen diffusion coefficient,

$$D_{K_i}^{\text{eff}} = \frac{2r}{3}\left(\frac{8RT}{\pi M_i}\right)^{0.5} \tag{106}$$

which is related to the gas molecules interacting with the pore walls and becomes significant as the pore radius (r) becomes smaller than the mean free path of the gas molecules. From the above equation, one can estimate the importance of Knudsen diffusion compared to standard diffusion for the various PEMFC porous media. Such a calculation is shown in Figure 11 (Nonoyama *et al.*, 2011), where it is clear that for the gas-diffusion layers Knudsen diffusion is not important, but for catalyst layers it is dominant due to the much smaller pore sizes. Finally, to calculate the pressure drop within the gas phase, Darcy's law (Equation (58)) is used.

The water generated at the cathode and the water dragged across the membrane from anode are transported to the flow channels in both liquid and vapor form. While the vapor form is accounted in multicomponent gas-phase transport equations, the transport of liquid water is usually done using Darcy's law (Equation (58)), which can be written in a flux form as

$$\mathbf{N}_{\text{w,L}} = -\frac{k_k}{\overline{V}_{\text{w}}\mu}\nabla p_{\text{L}} \tag{107}$$

The effective permeability, k_k, is a function of the absolute permeability which is a function only of the structure of the porous medium (same for both liquid and vapor phases). Typically, this value is determined experimentally, but the Carman–Kozeny equation can be used to estimate it or explore its dependence on porosity,

$$k_{\text{sat}} = \frac{\varepsilon_0^3}{(1-\varepsilon_0)^2 k' S_{\text{o}}^2} \tag{108}$$

where k' is the Kozeny constant and S_{o} is the specific surface area based on the solid's volume.

3.2.1 Multiphase flow

The above equations deal with the transport of the gas and liquid phases separately. However, these phases interact with each other for water in terms of the phase change and the calculation of a medium's effective properties, which is known as considering two phase or multiphase flow (an ice phase can also be considered for subzero operation and startup). To incorporate phase change, one can either assume equilibrium or use a rate equation. For the latter, a reaction equation of the form

$$r_{\text{evap}} = k_{\text{evap}} a_{\text{G,L}}\left(p_{\text{w}} - p_{\text{w}}^{\text{vap}}\right) \tag{109}$$

can be used, where k_{evap} is the reaction rate constant. This value just becomes source/sink terms in the material and energy balances (Equations (33) and (66), respectively).In typical fuel-cell porous media, the area

between the phases ($a_{G,L}$) and the reaction rate constant are sufficiently high that one can assume equilibrium between the liquid and vapor phases. Thus, the concentration of water in the vapor phase is the saturation pressure, which should be corrected for pore effects by the Kelvin equation

$$p_0^{vap} = p_{0,o}^{vap} \exp\left(\frac{p_C \overline{V}_w}{RT}\right) \tag{110}$$

where $p_{0,o}^{vap}$ is the uncorrected (planar) vapor pressure of water and is a function of temperature, and p_C is the capillary pressure,

$$p_C = p_L - p_G = -\frac{2\gamma \cos\theta}{r} \tag{111}$$

where r is the nominal pore size, γ is the surface tension of water, and θ is the internal contact angle that a drop of water forms with a solid. Equation (111) is based on how liquid water wets the material; hence, for a hydrophilic pore, the contact angle is $0° \leq \theta < 90°$, and for a hydrophobic one, it is $90° < \theta \leq 180°$.

In addition to replacing the gas-phase material balance with the saturation pressure, one can combine the transport equations for the liquid and vapor to just be a water one (i.e., there is an effective transport property composed of liquid and vapor coefficients). This combination can be done through just weighting the fluxes by the volume fraction that each phase occupies, which can be written in terms of the liquid saturation, S, which is the volumetric fraction of pore space that is occupied by liquid water; thus,

$$\varepsilon_G = \varepsilon_o(1 - S) \tag{112}$$

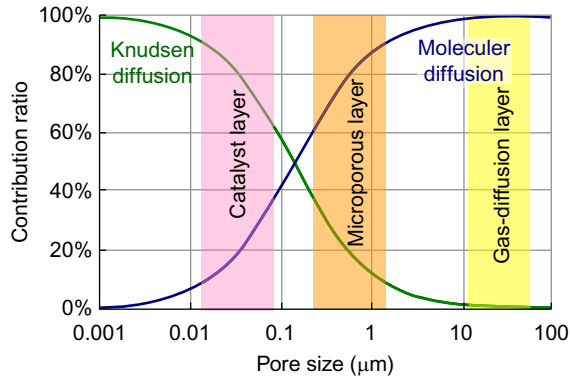

Figure 11 Relationship between domain pore size and the contribution ratio of molecular diffusion versus Knudsen diffusion of oxygen in nitrogen at 80°C, 150 kPa (Nonoyama *et al.*, 2011).

To determine the saturation, different models have been used, but for the approach above, one can use the experimental capillary-pressure–saturation relationship as shown in Figure 12. From the figure, one sees that addition of a hydrophobic (i.e., Teflon) treatment causes the curve to shift toward higher capillary pressures (i.e., more hydrophobic). Also, the gas-diffusion layer exhibits an intermediate wettability where there is a hysteresis between imbibition and drainage that spans p_C=0. However, this hysteresis is not as important since PEMFCs operate on the imbibition curve during operation (unless drying is being done), as water is always being injected from the catalyst layer to the gas channel. Similarly, the full curve is not expected to occur because the high permeability of tradition gas-diffusion layers means that once breakthrough and a dominant pore pathway has formed, it is sufficient for removing the liquid water assuming that the ribs do not block too much of the exit pathway.

The curve in Figure 12 can be used as input in a model to determine the transport properties within the porous medium, namely, the effective permeabilities of the phases,

$$k_k = k_{r,k} k_{\text{sat}} \tag{113}$$

where $k_{r,k}$ is the relative permeability for phase k. To use the capillary-pressure data, one can fit the curve using a Leverett-J function,

$$p_C = \gamma \cos\theta \left(\frac{\varepsilon_o}{k_{\text{sat}}}\right)^{0.5} J_{(S)} \tag{114}$$

Next, an expression for the relative permeability as a function of saturation can be used to calculate it. This expression is often a power law of the type,

$$k_{r,L} = S^n \tag{115}$$

with the power n typically between 2 and 5 and is determined through pore-network simulation or macroscopic modeling.

A less empirical way to treat the capillary-pressure data is to fit the curve using the separately measured pore-size distribution and a contact-angle distribution (Weber, 2010)

$$S^* = \int_0^{90} \Psi(\theta) \left\{ \sum_k \frac{f_{r,k}}{2} \left[1 + \text{erf}\left(\frac{\ln r_c - \ln r_{o,k}}{s_k \sqrt{2}} \right) \right] \right\} d\theta$$

$$+ \int_{90}^{180} \Psi(\theta) \left\{ \sum_k \frac{f_{r,k}}{2} \left[1 - \text{erf}\left(\frac{\ln r_c - \ln r_{o,k}}{s_k \sqrt{2}} \right) \right] \right\} d\theta$$

$$= \int_0^{90} \sum_n f_{\theta,n} \left\{ \frac{1}{\sigma_n \sqrt{2\pi}} \exp\left[-\frac{1}{2} \left(\frac{\theta - \theta_{o,n}}{\sigma_n} \right)^2 \right] \right\}$$

$$\left\{ \sum_k \frac{f_{r,k}}{2} \left[1 + \mathrm{erf} \left(\frac{\ln\left(-\frac{2\gamma \cos\theta}{p_C} \right) - \ln r_{o,k}}{s_k \sqrt{2}} \right) \right] \right\} \mathrm{d}\theta + \int_{90}^{180} \sum_k \ldots \qquad (116)$$

where $r_{o,k}$ and s_k are the characteristic pore size and spread of distribution k, respectively, and $f_{r,k}$ is the fraction of the total distribution made up of distribution k, where the $f_{r,k}$s sum to unity; the contact-angle distribution is given by

$$\Psi(\theta) = \sum_n f_{\theta,n} \left\{ \frac{1}{\sigma_n \sqrt{2\pi}} \exp\left[-\frac{1}{2} \left(\frac{\theta - \theta_{o,n}}{\sigma_n} \right)^2 \right] \right\} \qquad (117)$$

where $\theta_{o,n}$ and σ_n are the characteristic contact angle and deviation of distribution n. The integration in equation (116) is done with respect to the critical radius as determine from Equation (111)

$$r_c = -\frac{2\gamma \cos\theta}{p_C} \qquad (118)$$

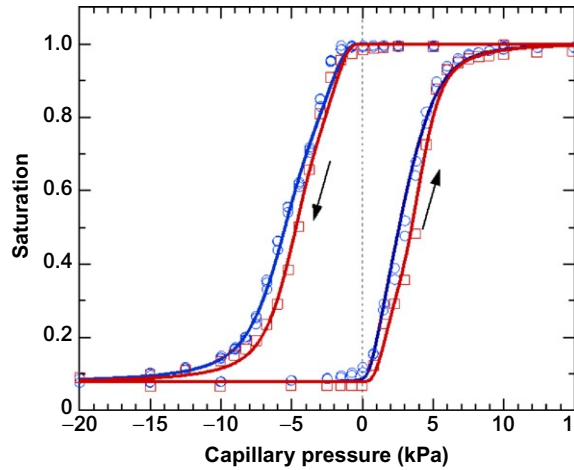

Figure 12 Capillary-pressure–saturation relationship for an SGL gas-diffusion layer with 0 (blue) and 5 wt.% (red) Teflon.

which is a function of hydrophobicity and thus the integral is separated into hydrophobic and hydrophilic contact angles, as the critical angle goes toward infinity at a zero capillary pressure. Finally, one can also incorporate the residual saturation, S_r, as shown in Figure 12

$$S = S_r + S^*(1 - S_r) \tag{119}$$

Using the above integration approach, one can also determine expressions for the relative permeability of the gas and liquid of

$$k_{r,L} = S_e^2 \frac{\begin{aligned}&\int_0^{90} \Psi(\theta) \left\{ \sum_k \frac{f_{r,k}}{2} r_{o,k}^2 \exp\left[2s_k^2\right] \left[1 + \operatorname{erf}\left(\frac{\ln r_c - \ln r_{o,k}}{s_k\sqrt{2}} - s_k\sqrt{2} \right) \right] \right\} d\theta \\ &+ \int_{90}^{180} \Psi(\theta) \left\{ \sum_k \frac{f_{r,k}}{2} r_{o,k}^2 \exp\left[2s_k^2\right] \left[1 - \operatorname{erf}\left(\frac{\ln r_c - \ln r_{o,k}}{s_k\sqrt{2}} \right) - s_k\sqrt{2} \right] \right\} d\theta\end{aligned}}{f_{HI} \left\{ \sum_k f_{r,k} r_{o,k}^2 \exp\left[2s_k^2\right] \right\} + (1 - f_{HI}) \left\{ \sum_k f_{r,k} r_{o,k}^2 \exp\left[2s_k^2\right] \right\}} \tag{120}$$

and

$$k_{r,G} = (1 - S)^2 \frac{\begin{aligned}&\int_0^{90} \Psi(\theta) \left\{ \sum_k \frac{f_{r,k}}{2} r_{o,k}^2 \exp\left[2s_k^2\right] \left[1 - \operatorname{erf}\left(\frac{\ln r_c - \ln r_{o,k}}{s_k\sqrt{2}} - s_k\sqrt{2} \right) \right] \right\} d\theta \\ &+ \int_{90}^{180} \Psi(\theta) \left\{ \sum_k \frac{f_{r,k}}{2} r_{o,k}^2 \exp\left[2s_k^2\right] \left[1 + \operatorname{erf}\left(\frac{\ln r_c - \ln r_{o,k}}{s_k\sqrt{2}} \right) - s_k\sqrt{2} \right] \right\} d\theta\end{aligned}}{f_{HI} \left\{ \sum_k f_{r,k} r_{o,k}^2 \exp\left[2s_k^2\right] \right\} + (1 - f_{HI}) \left\{ \sum_k f_{r,k} r_{o,k}^2 \exp\left[2s_k^2\right] \right\}} \tag{121}$$

respectively, where f_{HI} is given by

$$f_{HI} = \sum_n \frac{f_{\theta,n}}{2} \left[1 + \operatorname{erf}\left(\frac{90 - \theta_{o,n}}{\sigma_n\sqrt{2}} \right) \right] \tag{122}$$

and an effective saturation is used for the liquid relative permeability

$$S_e = \frac{S - S_r}{1 - S_r} \tag{123}$$

Finally, the above discussion is based on assuming that one can weight the liquid and vapor transport through the phase volume fractions. However, an alternative approach is to assume the equilibrium but actually calculate the separate liquid- and vapor-phase velocities. This approach is known as the multiphase mixture approach. In this analysis, although both liquid and vapor phases move simultaneously, they move at

different velocities. This difference leads to a drag on either phases. In this approach, the liquid-phase velocity is calculated using

$$\mathbf{v}_{\mathrm{L}} = \lambda_{\mathrm{L}} \frac{\rho_{\mathrm{m}}}{\rho_{\mathrm{L}}} \mathbf{v}_{\mathrm{m}} + \frac{k\lambda_{\mathrm{L}}(1-\lambda_{\mathrm{L}})}{\varepsilon_{\mathrm{o}} \rho_{\mathrm{L}} \nu_{\mathrm{m}}} [\nabla p_{\mathrm{C}} + (\rho_{\mathrm{L}} - \rho_{\mathrm{G}})\mathbf{g}] \tag{124}$$

where the subscripts m stands for the mixture, ρ_k and ν_k are the density and kinematic viscosity of phase k, respectively, and λ_{L} is the relative mobility of the liquid phase which is defined as

$$\lambda_{\mathrm{L}} = \frac{k_{r,\mathrm{L}}/\nu_{\mathrm{L}}}{k_{r,\mathrm{L}}/\nu_{\mathrm{L}} + k_{r,\mathrm{G}}/\nu_{\mathrm{G}}} \tag{125}$$

A similar equation can be derived for the gas-phase velocity, which is then used to get the pressure drop in the gas phase while the Stefan–Maxwell Equations (103) govern the diffusive transport of the gas species. In Equation (124), the first term represents a convection term, and the second comes from a mass flux of water that can be broken down as flow due to capillary phenomena and flow due to interfacial drag between the phases. The velocity of the mixture is basically determined from Darcy's law using the properties of the mixture. While the use of the multiphase mixture model does speed computational time and decreases computational cost, problems can arise if the equations are not averaged correctly.

It is worthwhile to examine the impact that accounting for phase change can have on PEMFC performance and the coupling between energy and material transport within the porous media. As the highest temperature in a PEMFC occurs within the cathode catalyst layer, the temperature gradient is from that layer out to the gas channel (see Figure 1). This temperature gradient causes a vapor-pressure gradient to develop, and if the gas is fully humidified, then water will be transported along that vapor-pressure gradient (i.e., water evaporates at the catalyst layer and transports in the gas phase through the porous media to the gas channel where it condenses). This phase-change-induced flow also is effective in moving heat from the catalyst layer to the gas channel due to the large latent heat of water.

To ascertain the impact of phase-change-induced flow, a back-of-the-envelope analysis is conducted using the Stefan–Maxwell Equations (38) for a given temperature gradient and operating temperature as shown in Figure 13. In the figure, the water flux is normalized such that current generation is equal to 1. Thus, it is apparent that only a couple of degrees are needed at the higher operating temperatures to move as much water as produced. Thus, this phenomenon is the dominant mode of water removal at higher temperatures and may even cause the cell water content to decrease at higher current densities because the heat generated

outpaces the water generation. However, while the water-removal characteristics are a benefit of phase-change-induced flow, the net flux of water vapor is now out of the cell, which can result in the gas-phase velocity also being out of the cell (see Equation (36)). In either case, the movement of the water vapor from the catalyst layer to the gas channel due to phase-change-induced flow represents a mass-transfer limitation in terms of getting oxygen to the catalyst layer as it now must diffuse against that flux. As shown in the simple calculation in Figure 13, this can decrease the oxygen reaching the catalyst layer significantly. Thus, as with most PEMFC water-management issues, phase-change-induced flow has both positive and negative aspects and is something that can be optimized (e.g., by using a porous medium with a different thermal conductivity).

3.2.2 Pore-network models

The analysis above stems from the use of a macrohomogeneous framework; however, this is not necessarily accurate in terms of the exact distribution of water within the cell porous media, especially the fibrous gas-diffusion layer. This is especially true since a lot of the above underpinnings are based on a concept of a bundle of cylindrical pores, which is not the case for a gas-diffusion layer (see Figure 10). To describe the movement of water throughout this structure, yet have computational efficiency to simulate the entire layer, one uses pore-network modeling. Such an approach allows one to model the pore-length scale and therefore account for the capillary driven processes and water distribution. However, it is still too computationally costly to account for all of the coupled physics including phase change, and for running in a complete cell simulation. Therefore, it is valuable to be used in a multiscaling approach wherein the pore-scale models yield the functional relationships required for the more macroscopic complete cell models (e.g., saturation, effective properties, etc.). In addition to pore-network models, one can also consider using more rigorous full-morphology and/or Lattice-Boltzmann modeling. However, these later simulation techniques are more computationally expensive and require more detailed knowledge of the internal structure and forces, without providing significantly more insight, especially for use in macroscopic simulations and with typical gas-diffusion-layer saturations around 0.1–0.3 (Vogel *et al.*, 2005).

A pore-network model utilizes a simplified description of the pore space within the gas-diffusion layer. Thus, one idealizes the geometry in terms of pores and nodes which are where the pores interconnect as shown in Figure 14 (Gostick, 2011; Medici and Allen, 2011). The throat lengths and sizes are taken from analysis of either theoretical (e.g., see

Figure 14a) or actual (e.g., X-ray computed tomographs) images of the gas-diffusion layer that are digitized and analyzed. The generated network is thus validated by comparison of calculated and measured parameters including the pore- and throat-size distribution data as well as measurements such as the capillary-pressure–saturation relationship. Water flow and distribution within the generated network (Figure 14b) are solved by a stepwise fashion from one point to another and thus is independent of the real-space discretization grid (i.e., it only depends on the network).

For modeling transport, the same governing equation and multiphase phenomena described above hold. For example, for liquid–water imbibition, the model examines at each intersection or node where the water

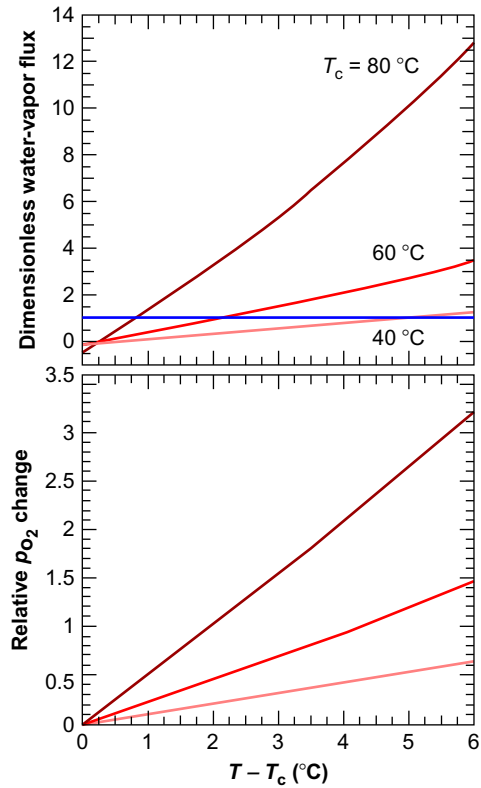

Figure 13 Back-of-the-envelope calculations using the Stefan–Maxwell equations showing the impact of phase-change-induced flow on the normalized (1=production, $i/2F$) water-vapor flux and relative change in oxygen partial pressure at the catalyst layer.

travels based on the local pressure and pore properties. The volumetric flowrate of water in a cylindrical pore of radius r_{ij} between nodes i and j (see Figure 14b) is governed by Poiseuille flow

$$q_{\mathrm{w,pore}} = A_{\mathrm{pore}} \cdot \mathbf{v}_{\mathrm{w,pore}} = \frac{\pi r_{ij}^4}{8\mu_{ij}^{\mathrm{eff}} l}\left(\Delta p_{ij} - p_{\mathrm{C}_{ij}}\right) \tag{126}$$

where Δp_{ij} is the pressure acting across the pore, l is the pore length, and $p_{\mathrm{C}_{ij}}$ is the capillary pressure in the pore when multiple phases are present. The volumetric flowrate exists only when $\Delta p_{ij} > p_{\mathrm{C}_{ij}}$. The effective viscosity within a pore, μ_{ij}^{eff}, is a function of the fluid position inside the pore, x_{ij}; the nonwetting (injected) fluid viscosity, μ_{nw}; and the wetting (displaced) fluid viscosity, μ_w. The effective viscosity is modeled to provide a smooth transition between the wetting and nonwetting viscosities while a pore is neither completely filled nor empty. The capillary pressure is also modeled as a function of the fluid position within each pore. It is calculated similar to Equation (111) but where either the average radius of the intersecting pores at each node or the radius of a given pore is used depending on where the water meniscus exists,

$$p_{\mathrm{C}_{ij}} = \gamma \cos\theta \left[\left(1 - \frac{r_i}{2\bar{r}_i} - \frac{r_j}{2\bar{r}_j}\right)\frac{1 - \cos\left(\frac{2\pi x_{ij}}{l}\right)}{r_{ij}} + \frac{1 + \cos\left(\frac{\pi x_{ij}}{l}\right)}{\bar{r}_i} + \frac{1 - \cos\left(\frac{\pi x_{ij}}{l}\right)}{\bar{r}_j}\right] \tag{127}$$

where $\bar{r}_i$ and $\bar{r}_j$ are the average pore radius around node i and j, respectively. The capillary pressure is zero when the pore is filled with only one fluid. Conservation of mass requires that the flowrate balances at each node for every simulation step; thus from Equation (126), one gets

$$\sum_j \frac{r_{ij}^4}{\mu_{ij}^{\mathrm{eff}}}\left(\Delta p_{ij} - p_{\mathrm{C}_{ij}}\right) = 0 \tag{128}$$

where the summation is over all of the pores connecting to the node (normally 4). The unknown pressure gradient, Δp_{ij}, is solved through the equation above. In addition to the pore sizes and lengths, one also needs the pore contact angle and fluid properties.

A sample output of a pore-network model is shown in Figure 15 (Medici and Allen, 2011). As can be seen, the model can show the distribution of the water, and in the top figure, one can see that a dominant pore pathway has formed. These distributions can then be used in other transport simulations to predict the gas-phase tortuosity and effective diffusion coefficients, which are needed the macroscopic modeling of

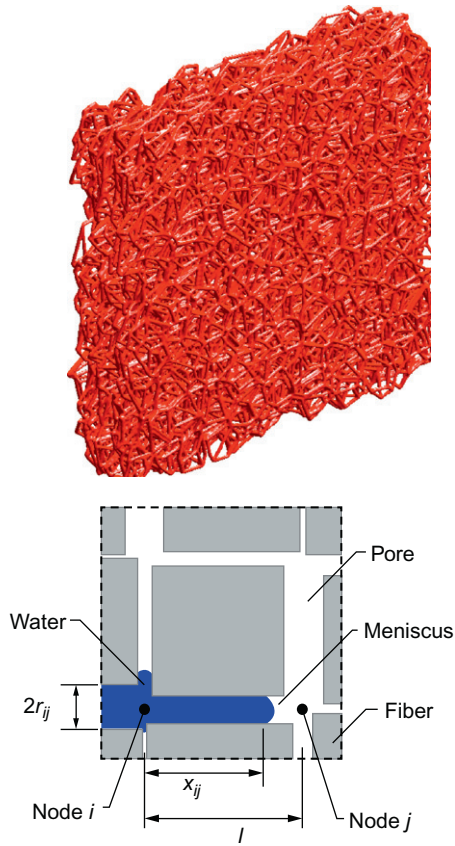

Figure 14 (a) Schematic of a computationally made carbon-fiber paper for use in a pore-network model (Gostick, 2011) and (b) schematic of a pore-network-model network (Medici and Allen, 2011).

the gas phase. More complicated pore-scale models can include phase change, impact of the microporous layers, ribs/channels, etc.

3.3 Catalyst layers

The catalyst layers, where the reduction (cathode) or oxidation (anode) reactions take place, are complex structures made of precious-metal catalysts like Pt or Pt-alloy nanoparticles supported on porous carbon, ionomer, and pores (see Figure 10). The complex structure provides pathways for the transport of reactant and product species, electrons, and protons to

the reaction sites. The catalyst layers, especially the cathode catalyst layer, hold the distinction of being host to most of the physical phenomena that occur in a PEMFC including everything discussed above. So, the membrane and porous-medium models must be solved with kinetic relations to describe the catalyst layer. The complex interplay of multiphysics at multiple length scale all within a layer of micron-level thickness makes catalyst layers the most complex of all the components to study, either experimentally or theoretically, within a PEMFC Optimization of catalyst layers attracts a lot of attention because of the significant expense of precious metals used and the hope to increase the effective utilization of fuels and durability.

Similar to the pore-network models, recently the catalyst layer has begun to be investigated in terms of microscopic modeling through direct numerical simulations. The idea is to either fabricate theoretically the catalyst layer or to use pictures of it in order to determine the various constituents and their locations as shown in Figure 16 (Epting *et al*., 2012; Pharoah *et al*., 2011). In the figure, one can see the pore space and the inverse of that which is the solid space composed of ionomer and secondary carbon particles or agglomerates where the reaction occurs. These agglomerates are typically on the order of tens of nanometer. By solving the transport equations in the given structures, one can determine the correct multiscaling expressions for use in the macroscopic simulations. Although in its infancy, this approach has great promise for helping to understand the phenomena occurring within the catalyst layer. For example, Figure 16c shows the oxygen-concentration distribution during operating where one can see the highly tortuous pathway of oxygen and the concentration change due to reaction, where the reaction seems to be occurring at the outside edges more than in the middle of the layer. The generation of these structures is beyond the scope of this chapter, although direct numerical simulations use essentially the same set of equations.

In addition to the kinetic equations describe above (e.g., Equation (23)), multiphase interactions and ion transport must be used. These are done by utilizing the models discussed in the preceding sections. Essentially, no new equations are required as the catalyst layer only involves adding the appropriate source terms to the material and energy balances (Equations (33) and (66), respectively). The only difference being that the source terms in the conservation equations include the contribution from the reactions. In addition, as the ionomer in the catalyst layer is not the sole component, the equations have to be modified to include the volume fraction, and the ionomer transport properties become effective properties where relations like the Bruggeman (see Equation (105)) one are used to scale them.

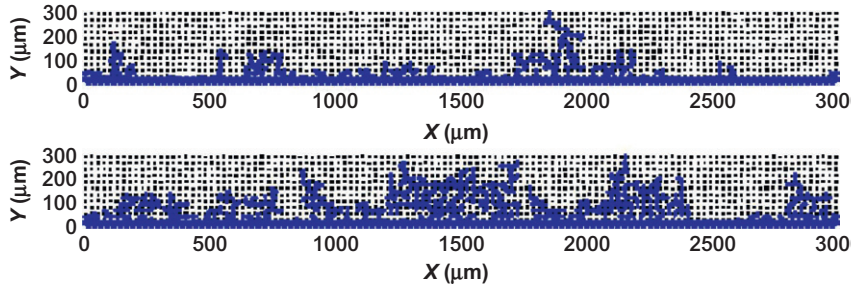

Figure 15 Water distributions at the time a capillary finger reaches the gas flow channel for two pore networks generated from the same pore-size distribution (Medici and Allen, 2011).

The catalyst layers are porous electrodes, which conceptually can be visualized as a resistor network as shown in Figure 17. Physically, the figure is showing that electron, proton, and kinetic resistances govern the reaction distribution. Thus, the overpotential and transfer current in the catalyst layer are functions of position because the current travels along the path of least resistance. The effect of concentration is accounted for in the calculation of the charge-transfer resistance, which is derived directly from the kinetic expressions as shown below. The figure also shows capacitors in parallel with the charge-transfer resistance, signifying charging of the double layers during transient operation. However, this typically occurs on very small time scales and can be neglected unless one is doing frequency-dependent analysis such as electrochemical impedance spectroscopy (EIS). Understanding the porous-electrode concept, one sees that in Figure 16c both the oxygen and protons seem to be limiting the reaction as it has a parabolic distribution, which is probably due to a higher operating current density (i.e., more mass-transfer resistance) and perhaps drier conditions where the ionomer in the catalyst layer is more resistive.

The kinetic expressions, Equations (26) and (29) for the HOR and ORR, respectively, result in a transfer current between the electronic-conducting (1) and ionic-conducting (2) phases (see Equation (33)), which is related to the current density in the two phases through Equation (43)

$$\nabla \cdot \mathbf{i}_2 = -\nabla \cdot \mathbf{i}_1 = a_{1,2} i_{h,1-2} \tag{129}$$

Assuming the ORR is the only reaction that is occurring in the cathode (i.e., crossover and degradation reactions are ignored) and there are no ionic impurities, the conservation Equation (33) for oxygen in the cathode can be written as

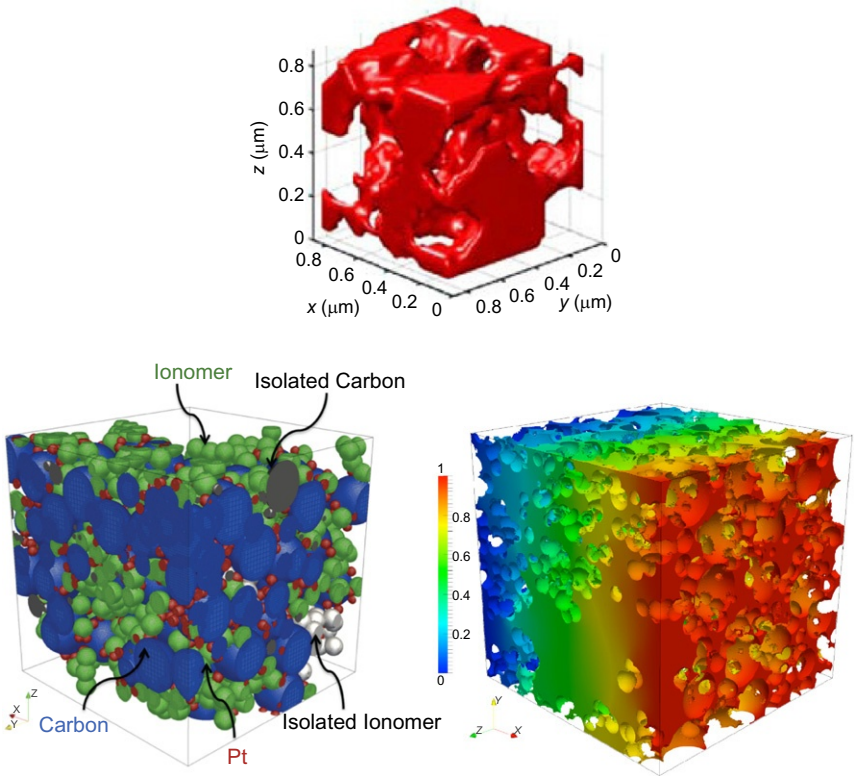

Figure 16 (a) Experimentally determined catalyst-layer macropore distribution from X-ray microtomography (Epting *et al.*, 2012), (b) computationally constructed catalyst layer, and (c) direct numerical simulation results for the oxygen concentration within that catalyst layer (Pharoah *et al.*, 2011).

$$\nabla\cdot\mathbf{N}_{O_2,G} = -\frac{1}{4F}a_{1,2}i_{0_{ORR}}(1-\Theta_{PtO})\left(\frac{p_{O_2}}{p_{O_2}^{ref}}\right)^{m_0}\exp\left(-\frac{\alpha_c F}{RT}(\eta_{ORR})\right)$$
$$= \frac{1}{4F}\nabla\cdot\mathbf{i}_1 \tag{130}$$

The interfacial area of the catalyst with respect to electrolyte and gaseous reactants, $a_{1,2}$, is often determined by

$$a_{1,2} = \frac{m_{Pt}A_{Pt}}{L} \tag{131}$$

where L is the thickness of the catalyst layer and m_{Pt} and A_{Pt} are the catalyst loading and surface area (which is determined experimentally, typically through a cyclic-voltammetry of hydrogen adsorption and desorption). This expression assumes a homogeneous distribution of electrocatalyst in the catalyst layer.

As noted, to model the catalyst layer does not require new equations, especially if one is modeling at the microscopic scale. However, for macroscopic simulations, one would like to use the microscopic phenomena but applied at the macroscopic scale. Such an effort can be achieved by using known scaling expressions (which are seldom available) or by modifying the transfer-current source term to account for diffusional losses at the agglomerate scale. In this structure, the reactant or product diffuses through the ionomer film surrounding the agglomerate particle and into the agglomerate itself where it simultaneously reacts and diffuses. First, the agglomerate part is discussed and then the film. It should be noted that due to the small size of the agglomerate, it is taken to be isopotential and isothermal.

The diffusion and reaction into a spherical agglomerate is given by the dimensionless equation (see Equation (33))

$$\frac{1}{z^2\left(r_{agg}+\delta_{film}\right)}\frac{d}{dz}\left(z^2 D_{O_2}^{eff}\frac{1}{\left(r_{agg}+\delta_{film}\right)}\frac{dc_{O_2}}{dz}\right)+\frac{1}{4F}a_{1,2}i_{ORR,1-2}=0 \quad (132)$$

where $z=r/(r_{agg}+\delta_{film})$, and r_{agg} is the agglomerate radius, δ_{film} is the film thickness and the effective diffusion coefficient is through the agglomerate. To understand the impact of the agglomerate, an effectiveness factor can be used, which is defined as the ratio of the actual reaction rate to the rate if the entire interior surface is exposed to the conditions outside of the particle

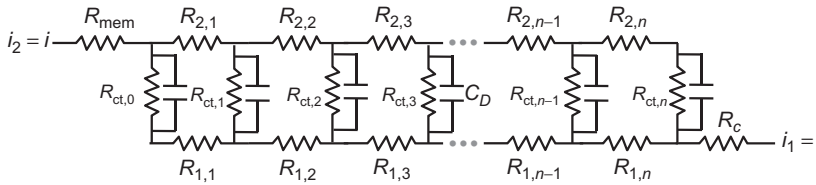

Figure 17 Simple equivalent-circuit representation of a porous electrode. The total current density, i, flows through the membrane and then the electrolyte phase (2) and the solid phase (1) including a contact resistance. In between, the current is apportioned based on the resistances in each phase and the charge-transfer resistances and double-layer charging.

$$E = \frac{4\pi r_{\text{agg}}^2 \left(-D_{\text{O}_2}^{\text{eff}} \frac{\text{d}c_{\text{O}_2}}{\text{d}r} |_{r=r_{\text{agg}}} \right)}{\frac{4}{3}\pi r_{\text{agg}}^3 \left(-k_{\text{s},m_0} c_{\text{O}_2,\text{s}}^{m_0} \right)} \tag{133}$$

where k_{s,m_0} is the reaction rate of the ORR at the surface conditions,

$$k_{\text{s},m_0} = \frac{a_{1,2} i_{0_{\text{ORR}}}}{4F c_{\text{O}_2}^{\text{ref}\, m_0}} (1 - \Theta_{\text{PtO}}) \exp\left(-\frac{\alpha_{\text{c}} F}{RT} \left(\eta_{\text{ORR},1-2} \right) \right) \tag{134}$$

Thus, one can write the transfer current as

$$\nabla \cdot \mathbf{i}_2 = a_{1,2} i_{h,1-2} E \tag{135}$$

For a first-order reaction (m_0=1), Equation (132) can be solved analytically to yield an effectiveness factor expression of

$$E = \frac{1}{\phi^2} (\phi \coth(\phi) - 1) \tag{136}$$

where ϕ is the dimensionless Thiele modulus

$$\varphi = r_{\text{agg}} \sqrt{\frac{k_{\text{s},m_0} C_{\text{O}_2,\text{s}}^{m_0 - 1}}{D_{\text{O}_2}^{\text{eff}}}} \tag{137}$$

which is a measure of the reaction rate to the diffusion rate. As discussed above, the ORR is not necessarily first order in oxygen concentration and is closer to m_0=0.8. Thus, Equation (136) is not rigorously valid. However, as shown in Figure 18 (Yoon and Weber, 2011), the error is minimal when Equation (136) is used as long as the correct concentration dependence is used in the Thiele modulus (Equation (137)). For the HOR, it is assumed to be first order in hydrogen (with no ionic contaminants) and thus Equations (135) and (136) hold with the appropriate HOR kinetic expression (see Equation (26)), and where

$$k_{\text{s,HOR}} = \frac{a_{1,2} i_{0_{\text{HOR}}}}{2F p_{\text{H}_2}^{\text{ref}}} \exp\left(\frac{\alpha_{\text{a}} F}{RT} (\Phi_1 - \Phi_2) \right) \tag{138}$$

and

$$\varphi = r_{\text{agg}} \sqrt{\frac{k_{\text{s,HOR}}}{D_{\text{H}_2}^{\text{eff}}}} \tag{139}$$

When accounting for diffusion through the film, one can use the permeation expression (Equation (84)) from the outside gas phase to the surface of the agglomerate

$$\text{N}_{\text{O}_2} = -D_{\text{film}} \nabla c_{\text{O}_2} = -\frac{D_{\text{film}} H}{RT} \nabla p_{\text{O}_2} = -\psi_{\text{O}_2,\text{film}} \nabla p_{\text{O}_2} \tag{140}$$

where H is Henry's constant and the film can be ionomer, liquid water, or perhaps both. Due to the thinness of the films, one can assume a linear flux; thus Equation (140) can be written as

$$N_{O_2} = \frac{p_{O_2,ext} - p_{O_2,surf}}{R_{O_2,film}} \tag{141}$$

where $R_{O_2,film}$ is the transport resistance of oxygen through ionomer film,

$$R_{O_2,film} = \frac{\delta_{film}}{\psi_{O_2}} \tag{142}$$

and is used since the film thickness and its transport properties are both unknown. While electron micrographs seem to suggest the film is on the order of nanometers, its transport properties are expected to much lower, especially in light of the interfacial resistance to transport that has been seen with these membranes.

At steady state, the flux given by Equation (140) is equal to the flux due to reaction and diffusion in the agglomerate; therefore, the unknown concentrations can be replaced. Using the resultant expression in the conservation, Equation (43) yields

$$\nabla \cdot \mathbf{i}_1 = 4F p_{O_2,ext}^{m_0} \left(\frac{1}{\frac{1}{R_{O_2,film}} + \frac{1}{k_{s,m_0} E}} \right) \tag{143}$$

and a similar one can be derived for the HOR. The above expression is the governing equation for the transfer-current density and includes both the film and agglomerate resistances. Upon inspection, one can see that as the current density increases (i.e., k_{s,m_0} increases), the film resistance becomes more significant and limiting. This is important because the drive for lower Pt loadings in the catalyst layer results in the current density per Pt site to increase to result in the same geometric current density. Thus, if the films are quite resistive to transport, which is expected, then they can become limiting, which essentially sets a lower bound on how low the Pt loading can become.

Finally, if there is liquid water in the catalyst layer, this is expected to block the reaction sites. While the multiphase equations discussed above account for this effect in terms of transport parameters, they do not in terms of reaction-site blockage. This latter effect can be addressed either by having a growing film of water over the agglomerate and using the approach above (i.e., Equation (143) with another film resistance) or one can use a more general approximation and use the saturation to scale the reaction area

$$a_{1,2} = a_{1,2}^{o}(1 - S) \tag{144}$$

where $a_{1,2}^{o}$ is the specific interfacial area with no water blockage.

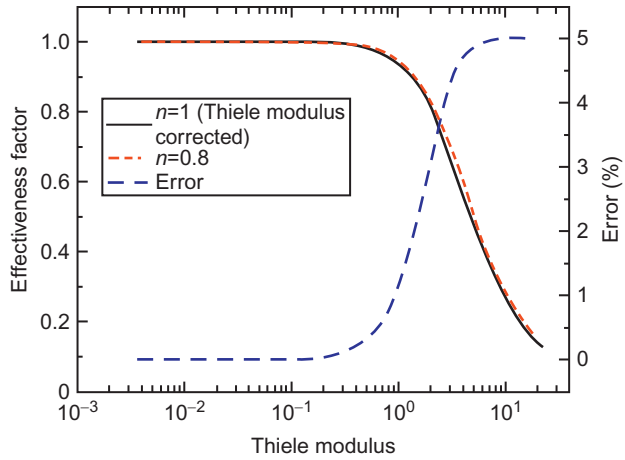

Figure 18 Comparison of the effectiveness factor from the analytic solution with Thiele modulus corrected for 0.8 reaction order (m_0), and the numerically calculated effectiveness factor for m_0=0.8.

3.4 Gas flow channels and flowfields

Gas flow channels or flowfields, as the name suggests, distribute gases for both electrodes, aid in transporting the product water out of the cell and give the cell, some mechanical reinforcement. They can also provide cooling and removal of the heat generated within the cell. The exact design and shape of the flowfield is very proprietary, with everything from multiple serpentine to parallel channels, to metal foams or meshes, to ones with holes, and to interdigitated designs.

In terms of modeling, gas-phase flow within the flow channels is relatively straightforward. One mainly uses the material balance (Equation (33)), Navier–Stokes (Equation (57)), and the energy-balance equations (66). One can use Ohm's law (Equation (52)) as well for electrons, but most flowfield materials are either graphite or metal and thus highly conductive and so an isopotential surface can be assumed. If desired, diffusional terms (e.g., Stefan–Maxwell (Equation (38)) or convective-diffusion (Equation (37)) equations) can be used with the Navier–Stokes equation; however, axial dispersion is normally negligible compared to pressure-driven flow. Finally, simpler flow equations are also often used such as assuming plug flow or Poiseuille flow. If only a pressure drop down the channel is required, correlations from fluid dynamics can be used to determine it (e.g., Ergun equation) (Bird *et al.*, 2002; McCabe *et al.*, 1993). For Navier–Stokes, flow is almost always laminar and one can use correlations to determine the

pressure drops in the flowfield structure similar to traditional flow in a pipe (Bird *et al.*, 2002; McCabe *et al.*, 1993), albeit with some changes due to varying density due to reaction in the orthogonal direction.

In terms of simulation, the flowfield can be considered in various multidimensional aspects as shown in Figure 19. In the figure, one can consider the full 3D structure, a 2D structure including the cell sandwich (see Figure 1) and the channel or the sandwich and the rib/channel, and there are also pseudodimensional methods where one considers changes along one of the dimension at the boundaries and not at every point within the domain. For the channel/rib dimension, only the boundary conditions need to be altered compared to just modeling the 1D cell sandwich, where the rib is the main conduit for thermal and electron conduction, and the channel is where the material exchanges occur. We believe that the optimal design in terms of computational expense and resolution need is a 1+2D where the rib/channel and cell dimensions are done rigorously, and the along-the-channel dimension is done only at the boundaries.

For the pseudo approach along the channel, it is necessary to only calculate the boundary conditions that need to be used for the 2D rib/channel and cell-sandwich modeling domain in each channel element as shown in Figure 20 for both a crossflow and coflow arrangement. These inputs include the gas composition, coolant temperature or input energy, and total pressure in the channel element. At the first element, the inlet composition, temperature, pressure, and total flux are given as boundary conditions. For the domains in Figure 20, the problem is essentially an initial-value one in the channel and thus one can march down the channel. Some iteration may be required if stoichiometric feeds are used in order to determine the average cell current density. For a counterflow arrangement, the problem becomes a boundary-value one; however, it is still often easier to guess the boundary conditions on one side and treat the problem as an initial-value one and iterate rather than try and relax to the solution.

A good use for the above approach is to determine where liquid water exists in the gas channel, or in other words, where the wet-to-dry and dry-to-wet transitions occur. The existence of liquid water in the gas channels complicates the analysis and worsens fuel-cell performance; a key aspect of modeling is the optimization of operation such that liquid water does not block reactant access. In extreme cases, complete blockage by water slugs can result in conditions of fuel starvation and hence carbon corrosion and durability concerns (Meyers and Darling, 2006).

Liquid water can exist within the gas channel as droplets or mist being carried along with the gas phase, (annular) films that flow in the corners and along the flowfield, and slugs which block the channel and cause

flow maldistribution and must be pushed out. These water mechanisms can be seen as a progression, where the blockage and slug flow occur as the film and droplets agglomerate due to liquid-water buildup. To model the water flow, the multiphase approaches described above can be used where the descriptions hold most for mist flows. For film and corner flows, one can model that as flow along a parallel plate (Bird *et al.*, 2002). For slug flow, the system becomes inherently dynamic where the pressure builds up and moves a slug, and then water accumulation or a surface (e.g., bend in a serpentine-flowfield channel) stops the slug until the pressure can increase again. This type of movement can be modeled using force balances as described below.

The above discussion centers on water that is in or condenses in the gas channel, but a major concern is removing liquid water from the surface of the gas-diffusion layer and into the channel. As seen in Figure 15, water droplets emerge from the gas-diffusion layer in defined locations, and the droplet will grow until it becomes of sufficient size to detach from the surface and either roll into a flowfield rib or be carried along with the gas velocity. To understand the process of detachment, a force-balance approach can be used

$$F_a + F_{\mathrm{p}} + F_{\mathrm{s}} + F_{\mathrm{g}} = 0 \tag{145}$$

where F_{a} is the adhesion or surface-tension force, F_{p} is the pressure force, F_{s} is the shear force acting on the droplet, and F_{g} is the gravity force, which is negligible for typical droplet sizes although can be more important for large slugs. The adhesion force is best determined experimentally using a sliding-angle technique with water penetration through the bottom of the gas-diffusion layer as this is more accurate than the use of a contact-angle-hysteresis type of measurement on the gas-diffusion-layer surface. The shear force can be calculated based on Stokes flow past a sphere and the shape of the droplet,

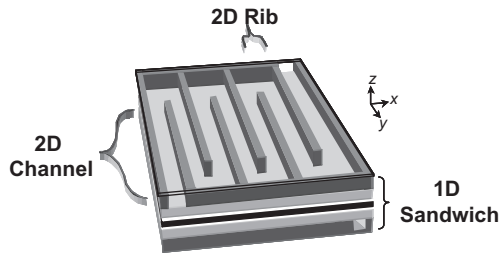

Figure 19 Fuel-cell schematic showing the different model dimensionalities: 1D models comprise the cell sandwich (*z* direction), 2D models comprise the 1D sandwich and either of the two other coordinate directions (*x* or *y*), and the 3D models comprise all three coordinate directions.

$$F_s = \left[\frac{6\mu H\langle v\rangle}{(H-h)^2}\right] d^2 \tag{146}$$

where d is the droplet diameter at its maximum, H is the channel height, $\langle v\rangle$ is the average flow velocity in the channel under laminar flow (Bird *et al.*, 2002), μ is the fluid viscosity, and h is the droplet height. Similarly, for the pressure force, one can derive an expression of the form

$$F_p = \left[\frac{a\mu d\langle v\rangle}{(H-h)^2}\right] [Hd] \tag{147}$$

where

$$a = 12\left[1 - \frac{192H}{\pi^5 W}\tanh\left(\frac{\pi W}{2H}\right)\right]^{-1} \tag{148}$$

where W is the channel width, and the above is fit from computational-fluid-dynamic simulations. The pressure force can also be used in a force balance on a water slug to determine when it will move. While the above equations can be used rigorously, they are valid only for a single droplet. For multiple droplets, interactions between them can occur and that is an area of active research.

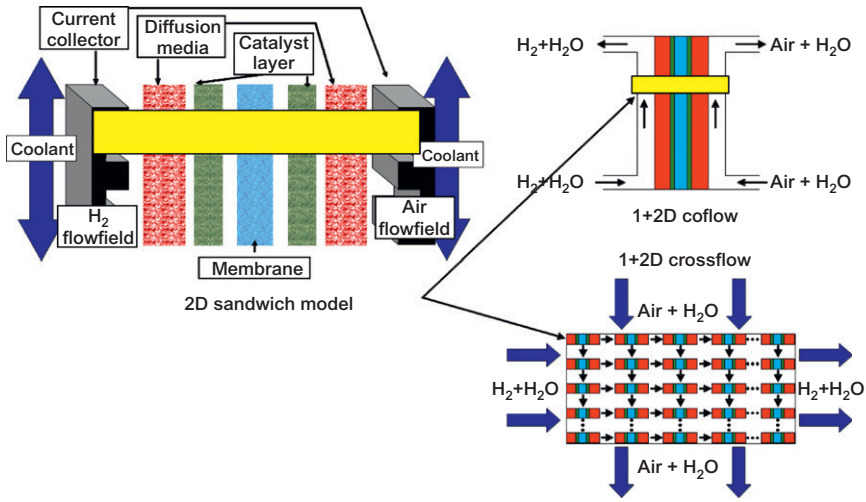

Figure 20 Schematic of the modeling domain where the 2D (through-plane with rib/channel) sandwich model (yellow box) is run along the gas channel in coflow or in a 2D matrix in crossflow.

3.5 Boundary conditions and summary

The previous sections described the various issues and methods to model PEFC phenomena. The governing conservation and transport equations along with important variables and constitutive relationships are summarized in Table 1 for reference. Due to the complexity and interconnectivity of the governing equations and constitutive relationships, most fuel-cell models are solved numerically. Although analytic solutions are obtainable in certain instances, these usually involve assumptions that make the solution of limited significance. For most numerically solved models, a control-volume approach is used. This approach is based on dividing the modeling domain into a mesh or grid. Using Taylor series expansions, the governing equations are cast in finite-difference form. Next, each conservation equation at the midpoints between adjacent mesh elements is summed and set equal to zero; hence, mass is rigorously conserved. This approach requires that all vectors be defined at half-mesh points, all scalars at full-mesh points, and all reaction rates at quarter-mesh points.

The various PEFC layers or domains are linked to each other through boundary conditions. There are two main types of boundary conditions, those that are internal and those that are external. The internal boundary conditions occur between layers inside the modeling domain, and the external ones are the conditions at the boundary of the entire modeling domain. Typically, coupled conditions are used for internal boundaries wherein the superficial flux and interstitial concentration of a species are made continuous. However, boundary conditions between the membrane and electrode can involve the fact that there is only ionic current in the membrane and electronic in the diffusion media (see Figure 17). Another common boundary condition is to have a change in concentration because a species dissolves; this is similar to the internal boundary condition in the membrane (i.e., interfacial resistance, Equation (85)) and is used sometimes where phases are not continuous across the boundary.

The external boundary conditions specify the concentrations and values for all the species and variables or their fluxes at the boundary. Examples include specifying the inlet conditions such as gas feed rates, composition, temperature, and humidity, or specifying the current density or potential, or specifying the thermal flux to the coolant stream. The external boundary conditions are often the same as operating conditions and therefore are very similar for most simulations, although there can be differences such as what condition is used for two-phase flow (e.g., zero saturation or zero capillary pressure). One of the most important and perhaps most complex boundary conditions is that between the gas-

diffusion layer and the flow channel in terms of liquid droplets, and it can have a substantial impact on water management and performance.

3.6 Impedance modeling

Electrochemical impedance spectroscopy (EIS) is often used as a diagnostic tool (Orazem and Tribollet, 2008). While powerful, with the capability to understand the various underlying transport properties and phenomena, the interpretation of the impedance spectra is highly dependent on its evaluation. The idea is that by applying only a small perturbation to the current during operation, the system response can be studied *in situ* and in a noninvasive way. Typically, a frequency range is scanned in order to acquire signatures for the different phenomena which occur with different time constants. EIS probes the various processes occurring throughout the entire cell.

The impedance works by perturbing the current or voltage and watching the response in the other. So, for a voltage oscillation of

$$E_t = E_0 \sin(\omega t) \tag{149}$$

the current response is phase shifted by ϕ to be

$$I_t = I_0 \sin(\omega t + \phi) \tag{150}$$

and the frequency-dependent impedance is given in terms of real and imaginary parts

$$Z(\omega) = \frac{E}{I} = Z_0(\cos\phi + j\sin\phi) \tag{151}$$

To analyze the data, often equivalent-circuit diagrams (e.g., see Figure 17) are drawn up and their various parameters (resistance, capacitance, etc.) then fit to the EIS spectra. For example, at high frequencies, the cell is short-circuited and thus the intercept of the EIS spectra with the real axis denotes the resistance through that short-circuit, which is often just a combination of the contact resistance and the membrane ionic resistance (see Figure 17), as the electronic resistance is minimal with standard

Table 1 Summary of key governing equations (number) and variables by phenomena and region

Variable	Property	Subdomain regions			
		Channel	Porous media	Catalyst layer	Membrane
Material	D_i^{eff}, ε	33	33	33, 42, 54	54
Temperature	$\hat{C}_{p_k}$, k_T	60	60	60	60
Current	κ	52	52	52, 23, 50	50
Velocity	μ, k	57	57, 58	57, 58, 54	54

PEMFC components. While this type of analysis can give some general characterizations, it is not that useful in terms of quantifying properties and phenomena beyond the high-frequency resistance.

The better approach is to use the same physic-based equations discussed above and take them into the frequency domain. Thus, for the variables of interest, one writes

$$x_i = \overline{x}_i + \mathrm{Re}\left\{\widetilde{x}_i e^{j\omega t}\right\} \tag{152}$$

and functions such as kinetic expressions become

$$\delta f = f(\overline{x} + \delta x) - f(\overline{x}) \approx f(\overline{x}) + \frac{\partial f}{\partial x}|_{x=\overline{x}}\delta x - f(\overline{x}) = \frac{\partial f}{\partial x}|_{x=\overline{x}}\delta x \tag{153}$$

Once the necessary transformations have been made, the impedance can be calculated by

$$Z = \frac{\widetilde{V}}{\widetilde{i}} \tag{154}$$

for each individual frequency. By using the governing equations and expressions, one can understand how each variable or property affects the impedance, or one can actually design an algorithm to fit the impedance by changing physical properties and parameters. As an example, one can start with a simplified material-balance Equation (33). In terms of computation, the transformations can be done numerically or analytically if possible, and essentially the number of unknowns doubles since each variable now has both a real and an imaginary component. Overall, impedance is a very powerful experimental tool, especially for characterization and trends, but its results are only as meaningful as the model used for its analysis.

4. OPTIMIZATION

The sections above set the stage in terms of the underlying governing equations and phenomena. A mathematical model of the entire cell, at a minimum of the cell sandwich, is capable of performing numerical optimization in terms of cell performance, and thus guiding experimental investigations. The performance of a fuel cell is affected by various parameters as seen above, such as cell operating parameters (pressure, temperature, utilization), geometric parameters and compositions (thicknesses, porosities, catalyst loadings), physical and kinetic properties (conductivity, diffusivity, permeability), etc. Some of these parameters, such as permeability and porosity, are controlled by the microstructure of the materials of the porous media. As these microstructure-sensitive parameters are somewhat mutually independent, the best approach for fuel-cell optimization is optimizing the individual macroscopic properties.

As described earlier, the performance of a fuel cell is always represented by a polarization curve (Figure 2); the key to the optimization process is improving the cell performance through reducing the various sources of potential loss. However, changing the macroscopic properties can have either a beneficial or a detrimental impact on fuel-cell performance and on the performance of the other system and cell components. These effects may be offsetting. For instance, changes in operating conditions may lower the cost of the cell but increase the cost of the surrounding system. Usually, compromises in the operating parameters are necessary to meet the application requirements, reduce the system cost, and achieve an acceptable cell durability. For example, an optimized design point for high current density will allow for a smaller cell size and lower capital cost to be used for the stack but result in lower system efficiency due to the lower cell voltage. This type of cell design would be beneficial for vehicle application, where lighter in weight and smaller in volume are important drivers for cost-effectiveness. Conversely, a fuel cell capable of operating at a lower current density but higher voltage would be more suitable for stationary backup-power operation. Optimization of the fuel cell often depends on the applications and operating point. Therefore, a clear understanding of the effects of these macroscopic properties and operating parameters on the cell performance is critical. It should be noted that at its heart, optimization is essentially a guided exploration of the sensitivity of the objective function (e.g., more current at a given potential) to controllable parameters.

4.1 Single-parameter optimization

In this section, some optimization results and case studies are examined that highlight the interplay of the various operating conditions and properties discussed above. In particular, each parameter is explored individually, thus allowing their sensitivity and impact to be determined at least initially.

4.1.1 Influence of cell operating conditions on performance

To optimize operating conditions, a basic understanding of their influence is required. Both temperature and pressure affect the composition of the incoming reactant gas streams, exchange current density, reversible cell potential, activation losses, transport properties, etc. When the temperature increases, the molar concentrations of fuel (hydrogen) and oxidant (oxygen) in the reactant streams decrease rapidly at low operating pressure, especially for humidified streams. However, the temperature effect on the reactant concentrations is less at elevated pressure. Conversely, the exchange current density and transport properties increase with temperature due to enhanced reaction kinetics and transport processes. In terms of the overall effect of temperature on cell

performance, a higher temperature is always beneficial for cell operation unless one approaches 100°C at ambient pressure. Temperature reduces both activation and ohmic losses, as shown in Figure 21 (Das *et al.*, 2007).

The effect of operating temperature on the polarization and power-density curves at 5atm pressure is provided in Figure 22 (Berning and Djilali, 2003). As shown in Figure 22, the maximum power density shifts toward higher current density with an increasing temperature because of reduced ohmic losses. Temperature, however, has less influence on the limiting current density at elevated pressure because the inlet gas composition changes little with temperature at elevated pressure. Changes in operating pressure, on the other hand, have a large impact on the inlet composition and, hence, on the limiting current density. A higher operating pressure and temperature are therefore best for fuel-cell operation. However, a higher pressure requires a higher pumping power for auxiliary systems, therefore necessitating optimization at the system level. A higher temperature may enhance degradation mechanisms, thereby causing durability and lifetime concerns.

Another important operating parameter for a fuel cell is the reactant utilization or stoichiometry. Stoichiometry represents the actual flow rate for the reactant delivered to the fuel cell or how much reactant is consumed in the fuel cell for a given amount of reactant supply. Stoichiometry and utilization are inversely proportional. In terms of reactant utilization, higher flowrates result in better fuel-cell performance. However, utilization of the fuel and oxidant involves trade-offs with respect to the optimum utilization for a given system. If the hydrogen flowrate is too high, then the efficiency will be low for a single-pass system (because not all of the hydrogen will have time to react), and if the flowrate is too low, then there may not be enough force to move water out of the anode gas channel. For typical PEMFC operation, the required stoichiometry is around 1.2, but when air is used instead of oxygen, a stoichiometry of 2.0 or higher is needed since it is more dilute. Although higher air flowrates result in better cell performance, the reactant flowrates are also a design variable not only at the cell level, but also at the stack level. Therefore, the pumping power needed to maintain a given flowrate should also be considered. A higher stoichiometry also provides a higher limiting current density; however, if a cell is running at the mid or low current-density range, then a higher stoichiometry will not be beneficial for cell operation, unless needed to remove liquid in the flowfields.

4.1.2 Influence of physical and transport properties on cell performance

The effect of physical and transport properties on the cell performance is always intricate, and optimization of these properties is strongly dependent on the application of the cell and something that modeling is ideally suited to tackle. Operating pressure and temperature do not have strong influence on the physical properties, such as porosity, thickness, composition, etc. However, operating pressure and temperature strongly influence the transport properties, such as conductivity, diffusivity, permeability, etc. From the optimization point of view, it is usually impossible to decouple their effects from those of the operating parameters.

Before optimizing, one must know how these properties affect the cell performance, that is, their sensitivity, since that allows for a more focused effort. For instance, although gas-diffusion layers transport both reactant gas and electrons, the former is much more limiting than the latter. Thus, although a thin layer would minimize ohmic losses from the electrons, it would not allow for efficient spreading of the reactant gases to the catalyst layer under the ribs, which is a more critical issue. Similarly, the size of the pores within a gas-diffusion layer also plays an important role on cell performance. A larger pore brings the benefit of lower transport resistance with the expense of reduced mechanical strength of the layer. The distribution of pore sizes can be a more important parameter than the total porosity since the specific volumes of the small and large pores regulate the different modes of gas and water transport.

Microporous layers are good examples of individual components that affect the entire cell. Not only do these layers aid in mass transfer, but they also protect the membrane from the gas-diffusion-layer fibers and inhibit the catalyst layer from penetrating into the gas-diffusion layer. The microporous-layer parameters directly affect PEMFC performance. Although the liquid-water flux toward the anode is enhanced when the following microporous-layer characteristics are used, smaller pore size, lower porosity, a larger thickness, and higher hydrophobicity (Pasaogullari *et al.*, 2005), each of these parameters has their own optimum. The use of the microporous layer improves performance at high current densities, but at low current densities, a gas-diffusion layer without microporous layer provides better performance. In addition, increasing microporous-layer thickness has been observed both in experiments and in simulations to increase performance up to a critical thickness (Paganin *et al.*, 1996; Weber and Newman, 2005a). The critical thickness arises mainly due to the trade-offs between increasing the liquid pressure and back flux versus increasing oxygen mass-transport limitations and ohmic drop. Essentially, one is trying to minimize the overall saturation in Figure 23 of the composite microporous-/gas-diffusion-layer structure without significantly increasing the composite's resistance.

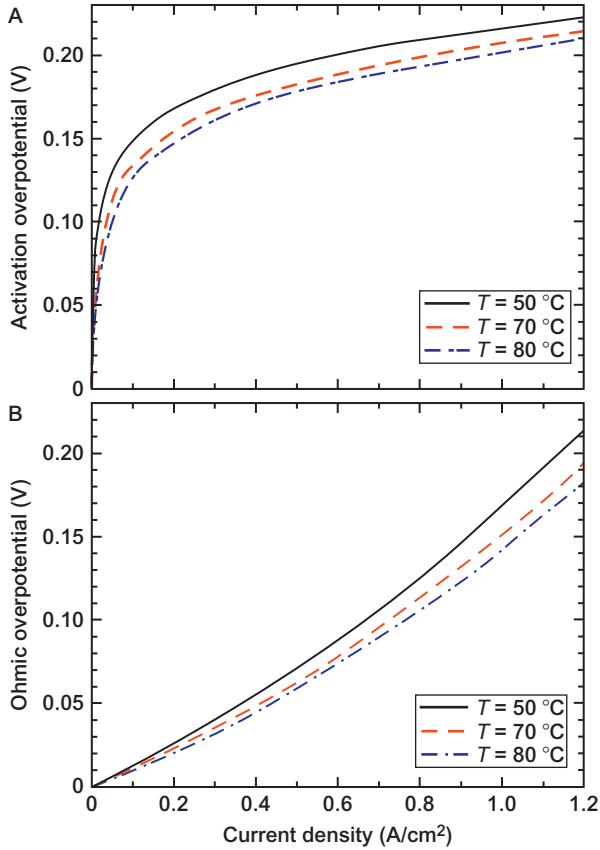

Figure 21 Effect of temperature on the activation and ohmic overpotentials (Das *et al.*, 2007).

However, if catalyst-layer flooding is limiting performance, then one does not want the microporous layer to be so resistive toward transport since, as shown in Figure 24, the cathode catalyst-layer saturation increases. For this case, it is beneficial if the microporous layer has some cracks or hydrophilic moieties such that water can escape from the catalyst layer in isolated points. Indeed, as shown in Figure 24, simulation results demonstrate that if only a portion (60%) of the microporous layer provides water to the GDL, with the rest having a very hydrophobic signature, then this provides for better oxygen transport at higher outlet capillary pressures and a lower propensity to flood. Also shown in

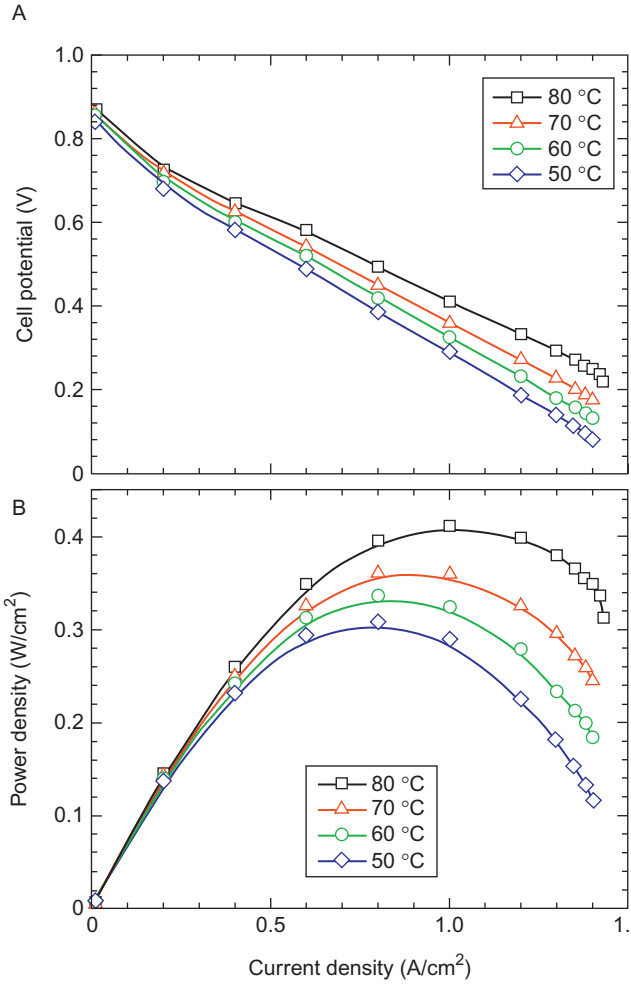

Figure 22 (a) Polarization and (b) power-density curves for different cell temperatures at 5atm pressure (Berning and Djilali, 2003).

the figure is the hypothetical case of taking the microporous layer and adding discrete water pathways, which allow for liquid connectivity between the water in the catalyst layer and that throughout the diffusion media to the channel. This results in a more linear response in the catalyst-layer capillary pressure, meaning that the saturation in the catalyst layer is lower.

Overall, the optimal microporous-layer properties are seen to be highly dependent on the coupled physical phenomena in the cell, and so their simulation requires careful consideration of all mechanisms and trade-offs involved. Finally, there is still a need to validate fully the role of a microporous layer, especially the impact it has on nonisothermal phenomena and vice versa, where phase-change-induced flow and the microporous layer's thermal conductivity become important, especially at higher operating temperatures.

Catalyst layers as discussed are critical in terms of optimizing performance and two parameters that are important are the amount of Pt and the amount of ionomer. A higher ionomer volume fraction in the catalyst layer is always favorable for the proton transport, but it brings a higher ohmic resistance. Since the volume fraction of all the constituents has to be unity, a higher ionomer content also results in a lower platinum content or a lower catalyst-layer porosity. In optimizing these parameters, one can optimize one parameter by fixing the other parameters. Single-parameter-based optimization will provide a good idea in terms of how each of these parameters affects the cell performance (i.e., the sensitivity of cell performance to these variables).

A typical single-parameter based optimization is shown in Figure 25 for ionomer volume fraction at a given cell potential of 0.6 V (Song *et al.*, 2004). The asymmetric broadness of Figure 25 indicates that although the current density is not very sensitive to the volume fraction near this optimal value (from 0.3 to 0.35), it is more sensitive to larger values of ionomer content than to lower values of ionomer content due to the impact that the ionomer content has on reducing the pore space for gas-phase transport.

The catalyst-layer thickness has an intricate influence on the cell performance as it is coupled with the transport resistance and the amount of Pt. A thicker CL increases the cell losses due to higher mass-transport resistances yet minimizes activation losses due to higher surface areas and amounts of Pt. Figure 26 shows the effect of the cathode catalyst-layer thickness on the cell output for a Pt loading of $0.2\,mg/cm^2$. For a given Pt loading, the cell potential increases rapidly with the increase of catalyst-layer thickness of lower than $10\,\mu m$, but it decreases slowly with the increase of the catalyst-layer thickness due to the limited rate of oxygen transport in the catalyst layer. In addition, as discussed above, ionomer-film resistances can become important for the thinner catalyst layers (see Equation (140)). Hence, an optimum catalyst-layer thickness for a given operating condition is crucial to achieve optimum PEMFC performance. Figure 26 shows the variation of current density with catalyst-layer thickness for a given cell potential of 0.8 V. It shows, with the increase of the catalyst-layer thickness, initially that the cell current density increases

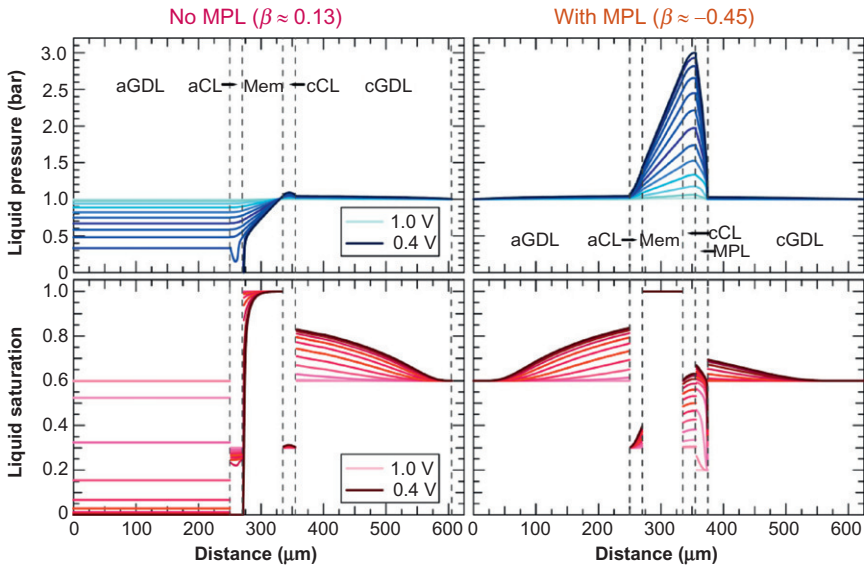

Figure 23 Isothermal simulations of a PEMFC with and without a microporous layer. Also given are the membrane net water flux per proton flux results. The various domains are noted, and the curves correspond to changes in potential going from 1 to 0.4 V in 50 mV increments. The simulation was at 60 °C, saturated feed gases (Weber and Newman, 2005a).

rapidly and then decreases slowly after reaching a certain thickness. Figure 26 also implies that the higher the Pt loading the wider the optimum zone of the catalyst-layer thickness and the higher the optimum catalyst-layer thickness. A fuel-cell design near the optimum zone will eventually decrease the cost with better cell performance.

4.2 Multiparameter optimization

Due to the interplay among the various PEFC components and phenomena, single-parameter optimization is of limited value since the optimizing over one property may change the optimum point of another. Thus, one should consider multiparameter-based optimization, where a group of parameters are optimized together. A very simple idea would be to iterate sequentially over multiple single-parameter optimizations such that for two variables, once an optimum is found in variable A, variable B is optimized, and then variable A is optimized, and so on until the optimums do not change. Such a method is straightforward but very time-consuming, especially for many variables.

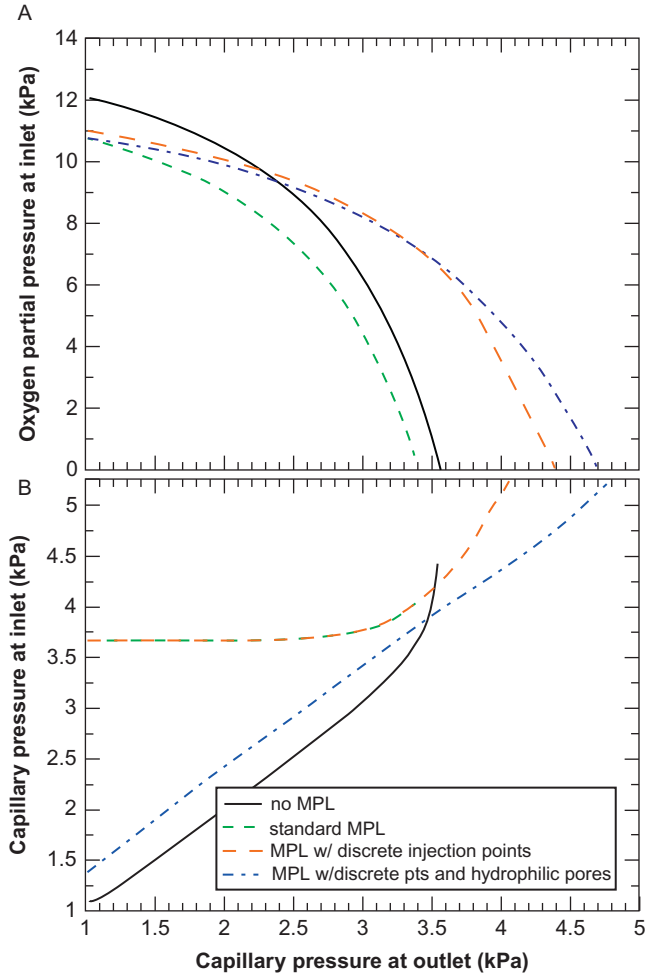

Figure 24 Calculated oxygen partial pressure (a) and capillary pressure (b) at the liquid-injection side (catalyst layer) as a function of the channel capillary-pressure boundary condition for different cases involving microporous layers (Weber, 2010).

When multiple design parameters are involved in the optimization process, parametric studies and graphical techniques are not feasible, and numerical-optimization methodologies are required for the optimization process. Numerical-optimization methods rely on analytical-sensitivity computations and gradient-based optimization algorithms. The goal or objective function of the multiparameter optimization can also vary

depending on the application area. It can be to improve the cell current density, to reduce the kinetic losses, or to improve the limiting current density. Since typical PEMFCs operate at midrange current densities, the goal of the optimization process is always to optimize the PEMFC performance with respect to the design parameters. Therefore, it is necessary to find the optimum design parameters that produce the maximum current density, and hence, the optimization problem can be formulated as (Das *et al.*, 2007; Secanell *et al.*, 2007; Song *et al.*, 2004)

$$\text{maximize } i \text{ at a given } V \quad \text{w.r.t.} \, \varepsilon_k^i, \delta^i, m_{\text{Pt}}, \%\text{Pt}, \text{ and } \%\text{PTFE}^i \tag{155}$$

and subject to

$$0 < \varepsilon_k^i < 1 \tag{156}$$

$$\sum \varepsilon_k^i = 1 \tag{157}$$

where i is the domain (gas-diffusion layer, etc.) and k is the phase. The constraints guarantee that the volume fraction of each one of the phases in the ith domain is not negative or larger than one, as well as the sum of all the volume fractions is one. Here the operating pressure and temperature are not needed because higher operating pressure and temperature are more or less always beneficial for cell-level performance.

The optimization objective function (cell current density at a given voltage) is not one of the governing unknowns that are mentioned in the governing transport equations. It is rather obtained during postprocessing. The current density per unit area of a fuel cell can be obtained

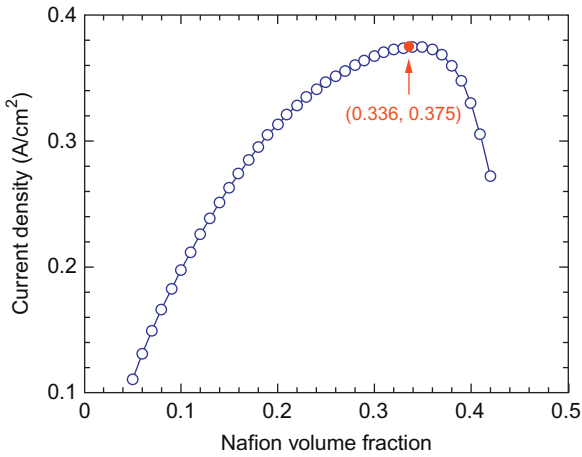

Figure 25 Optimization of ionomer content in the catalyst layer showing optimal point and current curve as a function of ionomer volume fraction (Song *et al.*, 2004).

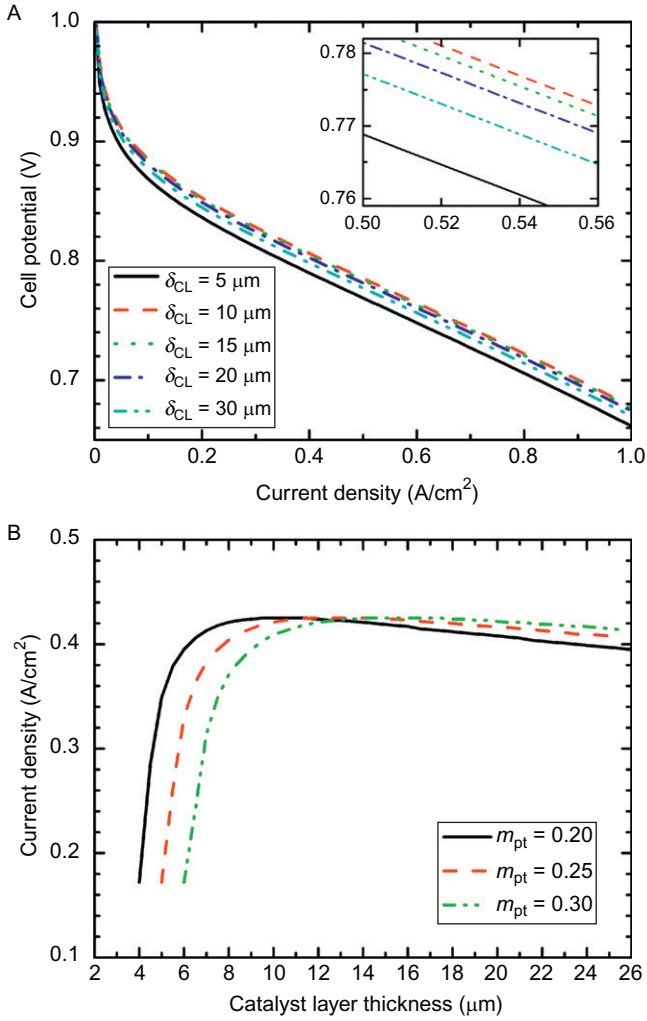

Figure 26 (a) Variation of the fuel-cell potential with current density for a platinum loading of 0.2 mg/cm^2 for different cathode catalyst-layer thicknesses and (b) optimization of cathode catalyst-layer thickness (Das *et al.*, 2007).

by integrating the volumetric current density over the unit volume of catalyst layer,

$$f(\mathbf{u},\mathbf{p}) = i\left(x_{O_2}, \varphi_s, \varphi_m; \varepsilon_k^i, \delta^i, m_{Pt}, \%Pt, \%PTFE\right) = \frac{1}{H}\int_0^H \int_0^L (\nabla \cdot i)\mathrm{d}x\mathrm{d}y \tag{158}$$

where $\mathbf{u}$ is the unknown vector, $\mathbf{p}$ is the vector of design parameters, H is the height of the catalyst layer, and L is the width of the catalyst layer.

The analytical sensitivities of the objective function f, with respect to any of the design variables p_i, can be obtained using functional analysis as (Secanell *et al.*, 2007)

$$\frac{\mathrm{d}f(\mathbf{u},\mathbf{p})}{\mathrm{d}p_i} = \frac{\partial f(\mathbf{u},\mathbf{p})}{\partial u_j}\frac{\partial u_j}{\partial p_i} + \frac{\partial f(\mathbf{u},\mathbf{p})}{\partial p_i} = \frac{1}{H}\int_0^H \int_0^L \left(\frac{\partial(\nabla \cdot i)}{\partial u_j}\frac{\partial u_j}{\partial p_i} + \frac{\partial(\nabla \cdot i)}{\partial p_i}\right)\mathrm{d}x\mathrm{d}y \tag{159}$$

where i is the index for number of independent variables for current density and j is the index for number of design parameters. The term $\partial u_j/\partial p_i$ is unknown and represents the change of the solution vector with respect to the design variables, which can be computed by solving the system of partial differential equations given by

$$\frac{\partial R(\mathbf{u},\mathbf{p})}{\partial u_j}\frac{\partial u_j}{\partial p_i} = -\frac{\partial R(\mathbf{u},\mathbf{p})}{\partial p_i} \tag{160}$$

where R is the governing fuel-cell transport equations. To solve the analytical-sensitivity equations of the objective function and constraints, these equations need to be discretized using a numerical program and solved with an optimization package, such as DAKOTA (Adams *et al.*, 2009). A flow chart of a multiparameter-based optimization is given in Figure 27. To obtain an optimal design, a prescription of an initial design is required to begin the optimization process. Then the inner loop solves the nonlinear governing transport equations using the initial design parameters, and the outer loop optimizes the design parameters to obtain an improved design.

A typical optimization history plot is shown in Figure 28, where Nafion volume fraction, ε_N; Pt loading, m_{Pt}; mass percentage of platinum catalyst, %Pt; and gas-diffusion layer porosity, ε_V^{gdl}; are optimized together for a given cell potential and with an initial design of $\mathbf{p} = \left\{\varepsilon_N, m_{Pt}, \%Pt, \varepsilon_V^{gdl}\right\} = \{0.3, 0.3, 0.2, 0.8\}$. Figure 28a shows that the maximum current density with the optimized design parameters is about $0.58\,A/cm^2$. The initial overpotential curve and the optimized overpotential curve are given in Figure 28b at a given voltage drop of 0.3 V. Note that there is not a guarantee that the performance improvements shown

in Figure 28b obtained by optimizing the design at this overpotential will be achieved over the entire polarization curve.

5. SUMMARY

There are many complex phenomena that occur with PEFCs, and mathematical modeling is ideally suited toward understanding the trade-offs and operation of the various interactions. In this chapter, the controlling equations for mainly performance-related issues have been examined, as durability and controls are covered elsewhere in this book. The governing transport and conservation equations have been detailed for the various fuel-cell regions, including discussion of some recent topics of interest such as multi-ion transport in membranes, multiphase flow in the porous media, ionomer films in the catalyst layer, and liquid-droplet removal into the gas channels. In addition, some model implementation scenarios and discussion on optimization using models have been made.

NOMENCLATURE

ENGLISH

a_i^{α}	activity of species i in phase α
$a_{k,p}$	interfacial surface area between phases k and p per unit volume, cm^{-1}
$a_{1,2}^{o}$	interfacial area between the electronically conducting and membrane phases with no flooding, cm^{-1}
A_{agg}	specific external surface area of the agglomerate, cm^{-1}
A_{Pt}	reactive surface area of platinum, cm^2/g
b	Tafel slope, V
$c_{i,k}$	interstitial concentration of species i in phase k, mol/cm^3
c_T	total solution concentration or molar density, mol/cm^3
$\hat{C}_{p_k}$	heat capacity of phase k, J/gK
d_i	driving force per unit volume acting on species i in phase k, J/cm^4
D_i	Fickian diffusion coefficient of species i in a mixture, cm^2/s
D_S	capillary diffusivity, cm^2/s
$D_{i,j}$	diffusion coefficient of i in j, cm^2/s
D_{K_i}	Knudsen diffusion coefficient of species i, cm^2/s
E	effectiveness factor
F	Faraday's constant, 96,487C/equiv.

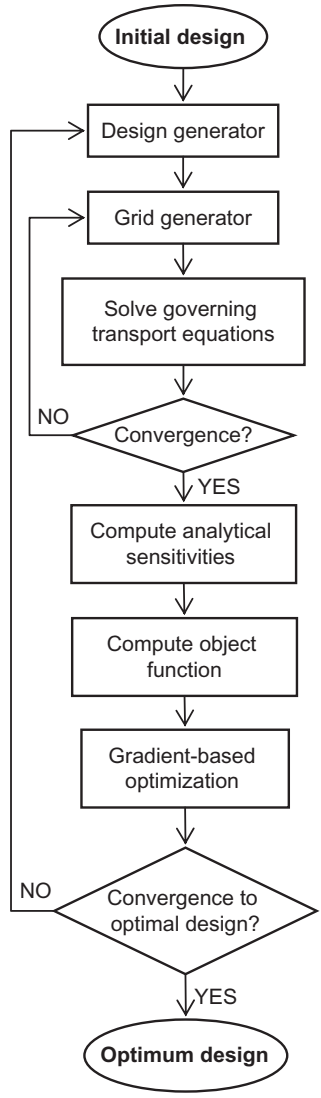

Figure 27 Implementation of the multiparameter optimization framework.

g	acceleration due to gravity, cm/s^2
$h_{k,p}$	heat-transfer coefficient between phases k and p, J/cm^2sK
H_i^f	heat of formation of species i
$\overline{H}_{i,k}$	partial molar enthalpy of species i in phase k, J/mol

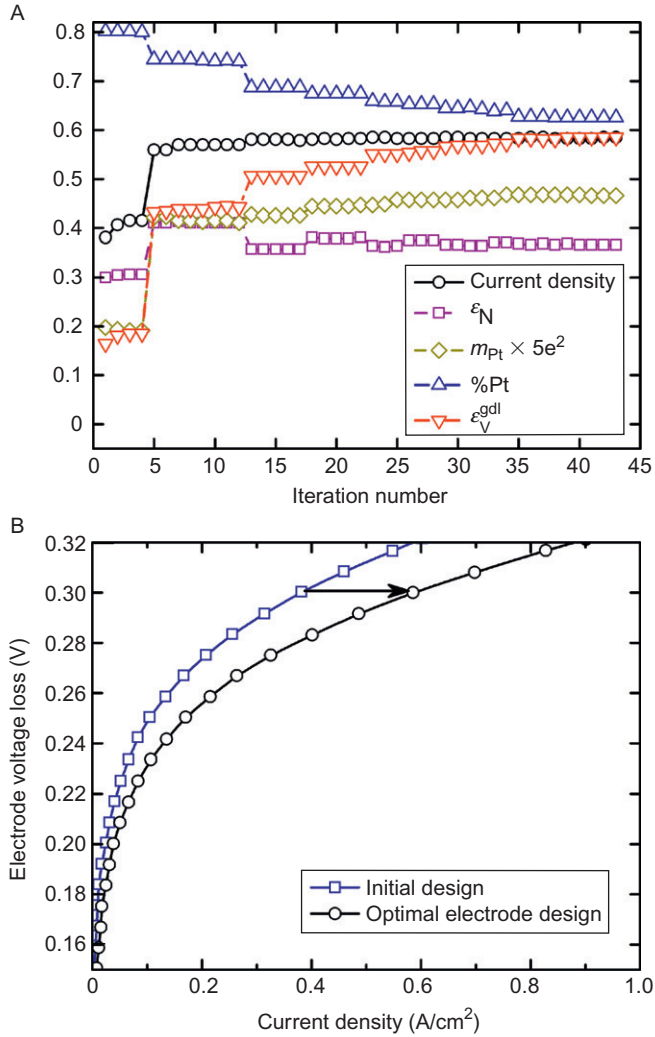

Figure 28 (a) Optimization history plot for the combined catalyst layer and gas-diffusion layer optimization, and (b) total overpotential curves for the initial and optimum designs (Secanell *et al.*, 2007).

$H_{i,j}$	Henry's constant for species i in component j, mol/cm^{3}kPa
ΔH_l	heat or enthalpy of reaction l, J/mol
i	superficial current density through the membrane, A/cm^2
i_k	current density in phase k, A/cm^2
i_{0_h}	exchange current density for reaction h, A/cm^2

$i_{h,k-p}$	transfer-current density of reaction h per interfacial area between phases k and p, A/cm^2
i_{lim}	limiting current density, A/cm^2
$J_{i,k}$	flux density of species i in phase k relative the mass-average velocity of phase k, mol/cm^{2}s
k	effective hydraulic permeability, cm^2
k'	ORR rate constant, s^{-1}
k^*	ORR rate constant, cm/s
k_{T_k}	thermal conductivity of phase k, J/cm^{2}K
k_{r}	relative hydraulic permeability
k_{sat}	saturated hydraulic permeability, cm^2
k_{Φ}	electrokinetic permeability, cm^2
L	catalyst-layer thickness, cm
m	parameter in polarization equation
m_{Pt}	loading of platinum, g/cm^2
M_i	molecular weight of species i, g/mol
$M_i^{z_i}$	symbol for the chemical formula of species i in phase k having charge Z_i
n	parameter in 0D model equation for polarization curve
n_h	number of electrons transferred in electrode reaction h
$\mathbf{N}_{i,k}$	superficial flux density of species i in phase k, mol/cm^{2}s
p_i	partial pressure of species i, kPa
p_{C}	capillary pressure, kPa
p_k	total pressure of phase k, kPa
$p_{\text{w}}^{\text{vap}}$	vapor pressure of water, kPa
q_k	superficial heat flux through phase k, J/cm^{2}s
Q	total amount of heat generated, J/cm^{2}s
Q_{k-p}	heat flux transferred between phases k and p, J/cm^{3}s
r	pore radius, cm
r_{evap}	rate of evaporation, mol/cm^{3}s
$R_{l,k-p}$	rate of reaction l per unit of interfacial area between phases k and p, mol/cm^{2}s
R	ideal-gas constant, 8.3143J/molK
R_{agg}	agglomerate radius, cm
$R_{g,k}$	rate of homogenous reaction g in phase k, mol/cm^{3}s
$R_{i,j}$	resistance of resistor i,j, Ωcm^2
R'	total ohmic resistance, Ωcm^2
$\mathfrak{R}_{i,k}$	total rate of reaction of species i in phase k, mol/cm^{3}s
$s_{i,k,l}$	stoichiometric coefficient of species i in phase k participating in reaction l
S	liquid saturation
$\overline{S}_{i,k}$	molar entropy of species i in phase k, J/molK
ΔS_h	entropy of reaction h, J/molK

t	time, s
T	absolute temperature, K
T_k	absolute temperature of phase k, K
u_i	mobility of species i, $cm^2 mol/Js$
U_h	reversible cell potential of reaction h, V
U'	potential intercept for a polarization equation, V
U_h^0	standard potential of reaction h, for oxygen reduction, 1.229V at 25°C
U_{H_h}	enthalpy potential, V
v_k	superficial velocity of phase k, cm/s
V	cell potential, V
$\overline{V}_i$	(partial) molar volume of species i, cm^3/mol
$W_{O_2}^{\text{diff}}$	molar flow rate of oxygen to the agglomerate, $mol/cm^3 s$
x	distance across the flowfield, cm
$x_{i,k}$	mole fraction of species i in phase k
y	distance along the flowfield channel, cm
z	distance across the cell sandwich, cm
z_i	valence or charge number of species i

GREEK

α_a	anodic transfer coefficient
α_c	cathodic transfer coefficient
α_w	water transport coefficient, $mol^2/Jcms$
β	net water flux per proton flux through the membrane
δ_n	diffusion length or thickness of region n, cm
ε_k	volume fraction of phase k
ε_o	bulk porosity
ϕ	Thiele modulus
Φ_k	potential in phase k, V
γ	surface tension, N/cm
$\eta_{h,k-p}$	electrode overpotential of reaction h between phases k and p, V
η^*	dimensionless overpotential
Π_h	Peltier coefficient for charge-transfer reaction h, V
κ	conductivity of the ionically conducting phase, S/cm
λ	moles of water per mole of sulfonic-acid sites
λ_L	relative mobility of the liquid phase
μ	viscosity, Pas
μ_i	(electro)chemical potential of species i, J/mol
μ_i^α	electrochemical potential of species i in phase α, J/mol
σ_o	standard conductivity in the electronically conducting phase, S/cm

v_k	kinematic viscosity of phase k, cm^2/s
θ	contact angle, degrees
ρ_k	density of phase k, g/cm^3
τ	stress tensor, kPa
τ_k	tortuosity of phase k
ξ	electroosmotic coefficient
ψ	Dimensionless parameter
ζ	characteristic length, cm

SUBSCRIPTS/SUPERSCRIPTS

1	electronically conducting phase
2	ionically conducting phase
agg	agglomerate
CL	catalyst layer
eff	effective value, corrected for tortuosity and porosity
ext	external to the control volume
f	fixed ionic site in the membrane
film	film covering the agglomerate
g	homogeneous reaction number
G	gas phase
h	electron-transfer reaction number
HOR	hydrogen-oxidation reaction
i	generic species
j	generic species
k	generic phase
l	heterogeneous reaction number
L	liquid phase
m	mixture
ORR	oxygen-reduction reaction
p	generic phase
ref	parameter evaluated at the reference conditions
s	solid phases
w	water

ACKNOWLEDGMENTS

The authors would like to thank Dr. Kai Sundmacher for his invitation to write this chapter. This work was funded by the Assistant Secretary for Energy Efficiency and Renewable Energy, Office of Fuel Cell Technologies, of the U.S. Department of Energy under contract number DE-AC02-05CH11231. P. K. D. also acknowledges the support of a Natural Sciences and Engineering Research Council of Canada's Postdoctoral Fellowship.

REFERENCES

Adachi, M., Navessin, T., Xie, Z., Frisken, B. and Holdcroft, S., *J. Electrochem. Soc.* **156,** B782 (2009).

Adams, B.M., Bohnhoff, W.J., Dalbey, K.R., Eddy, J.P., Eldred, M.S., Gay, D.M., Haskell, K., Hough, P.D. and Swiler, L.P., DAKOTA, A Multilevel Parallel Object-Oriented Framework for Design Optimization, Parameter Estimation, Uncertainty Quantification, and Sensitivity Analysis: Version 5.0 User's Manual, Sandia Technical Report SAND2010−2183, December 2009.

Appleby, A. J., *J. Electrochem. Soc.* **117,** 328 (1970).

Bear, J., Dynamics of Fluids in Porous Media. Dover Publications, Inc., New York (1988).

Berning, T. and Djilali, N., *J. Power Sources* **124,** 440 (2003).

Berning, T., Lu, D. M. and Djilali, N., *J. Power Sources* **106,** 284 (2002).

Bird, R. B., Stewart, W. E. and Lightfoot, E. N., Transport Phenomena. John Wiley & Sons, New York (1960).

Bird, R. B., Stewart, W. E. and Lightfoot, E. N., Transport Phenomena. 2nd ed. John Wiley & Sons, Inc., New York (2002).

Bontha, J. R. and Pintauro, P. N., *Chem. Eng. Sci.* **49,** 3835 (1994).

Booth, F. J., *J. Chem. Phys.* **19,** 391 (1951).

Bruggeman, D. A. G., *Ann. Phys.* **24,** 636 (1935).

Burlatsky, S. F., Atrazhev, V., Cipollini, N., Condit, D. and Erikhman, N., *ECS Trans.* **1,** 239 (2006).

Caremans, T. P., Loppinet, B., Follens, L. R. A., van Erp, T. S., Vermant, J., Goderis, B., Kirschhock, C. E. A., Martens, J. A. and Aerts, A., *Chem. Mater.* **22,** 3619 (2010).

Darling, R. M. and Meyers, J. P., *J. Electrochem. Soc.* **150,** A1523 (2003).

Darling, R. M. and Meyers, J. P., *J. Electrochem. Soc.* **152,** A242 (2005).

Das, P. K., Li, X. and Liu, Z. S., *J. Electroanal. Chem.* **604,** 72 (2007).

Dullien, F. A. L., Porous Media: Fluid Transport and Pore Structure. 2nd ed. Academic Press, Inc., New York (1992).

Epting, W. K., Gelb, J. and Litster, S., *Adv. Funct. Mater.* **22,** 555 (2012).

Fuller, T. F., Solid-polymer-electrolyte Fuel Cells Berkeley. University of California, California, USA (1992).

Gostick, J. T., *ECS Trans.* **41,** 125 (2011).

Gottesfeld, S., *ECS Trans.* **6,** 51 (2008).

He, Q., Lucas, I. T., Kusoglu, A., Weber, A. Z. and Kostecki, R., *J. Phys. Chem. B* **115,** 11650 (2011).

Kinoshita, K., Electrochemical Oxygen Technology. John Wiley & Sons, Inc., New York (1992).

Kreuer, K. D., Paddison, S. J., Spohr, E. and Schuster, M., *Chem. Rev.* **104,** 4637 (2004).

Kusoglu, A., Kienitz, B. L. and Weber, A. Z., *J. Electrochem. Soc.* **158,** B1504 (2011).

Lampinen, M. J. and Fomino, M., *J. Electrochem. Soc.* **140,** 3537 (1993).

Liu, W. and Zuckerbrod, D., *J. Electrochem. Soc.* **152,** A1165 (2005).

Mazumder, S. and Cole, J. V., *J. Electrochem. Soc.* **150,** A1503 (2003).

McCabe, W. L., Smith, J. C. and Harriott, P., Unit Operations of Chemical Engineering. 5th ed. McGraw Hill, Inc., New York (1993).

Medici, E. F. and Allen, J. S., *ECS Trans.* **41,** 165 (2011).

Meyers, J. P. and Darling, R. M., *J. Electrochem. Soc.* **153,** A1432 (2006).

Newman, J. and Thomas-Alyea, K. E., Electrochemical Systems. 3rd ed. John Wiley & Sons, New York (2004).

Neyerlin, K. C., Gu, W. B., Jorne, J. and Gasteiger, H. A., *J. Electrochem. Soc.* **153,** A1955 (2006).

Neyerlin, K. C., Gu, W. B., Jorne, J. and Gasteiger, H. A., *J. Electrochem. Soc.* **154,** B631 (2007).

Nonoyama, N., Okazaki, S., Weber, A. Z., Ikogi, Y. and Yoshida, T., *J. Electrochem. Soc.* **158,** B416 (2011).

Orazem, M. E. and Tribollet, B., Electrochemical Impedance Spectroscopy Hoboken. John Wiley and Sons, Inc., New Jersey (2008).
Paganin, V. A., Ticianelli, E. A. and Gonzalez, E. R., *J. Appl. Electrochem.* **26,** 297 (1996).
Parthasarathy, A., Dave, B., Srinivasan, S., Appleby, A. J. and Martin, C. R., *J. Electrochem. Soc.* **139,** 1634 (1992a).
Parthasarathy, A., Srinivasan, S., Appleby, A. J. and Martin, C. R., *J. Electronanal. Chem.* **339,** 101 (1992b).
Pasaogullari, U., Wang, C. Y. and Chen, K. S., *J. Electrochem. Soc.* **152,** A1574 (2005).
Paulus, U. A., Schmidt, T. J., Gasteiger, H. A. and Behm, R. J., *J. Electronanal. Chem.* **495,** 134 (2001).
Perry, R. H. and Green, D. W., Perry's Chemical Engineers' Handbook. 7th ed. McGraw-Hill, New York (1997).
Pharoah, J. G., Choi, H.-W., Chueh, C.-C. and Harvey, D. B., *ECS Trans.* **41,** 221 (2011).
Pintauro, P. N. and Bennion, D. N., *Ind. Eng. Chem. Fundam.* **23,** 230 (1984).
Pintauro, P. N. and Verbrugge, M. W., *J. Membr. Sci.* **44,** 197 (1989).
Reiser, C. A., Bregoli, L., Patterson, T. W., Yi, J. S., Yang, J. D. L., Perry, M. L. and Jarvi, T. D., *Electrochem. Solid State Lett.* **8,** A273 (2005).
Secanell, M., Carnes, B., Suleman, A. and Djilali, N., *Electrochim. Acta* **52,** 2668 (2007).
Shibata, S. and Sumino, M. P., *J. Electronanal. Chem.* **193,** 135 (1985).
Song, D. T., Wang, Q. P., Liu, Z. S., Navessin, T., Eikerling, M. and Holdcroft, S., *J. Power Sources* **126,** 104 (2004).
Stamenkovic, V. R., Mun, B. S., Arenz, M., Mayrhofer, K. J. J., Lucas, C. A., Wang, G., Ross, P. N. and Markovic, N. M., *Nat. Mater.* **6,** 241 (2007).
Uribe, F. A., Springer, T. E. and Gottesfeld, S., *J. Electrochem. Soc.* **139,** 765 (1992).
Vogel, H. J., Tolke, J., Schulz, V. P., Krafczyk, M. and Roth, K., *Vadose Zone J.* **4,** 380 (2005).
Wang, J. X., Springer, T. E. and Adzic, R. R., *J. Electrochem. Soc.* **153,** A1732 (2006).
Wang, J. X., Zhang, J. and Adzic, R. R., *J. Phys. Chem. A* **111,** 12702 (2007).
Weast, R. C. (Ed.) CRC Handbook of Chemistry and Physics, 59th ed. CRC Press, Boca Raton, FL (1979).
Weber, A. Z., *J. Power Sources* **195,** 5292 (2010).
Weber, A. Z. and Newman, J., *J. Electrochem. Soc.* **152,** A677 (2005a).
Weber, A. Z. and Newman, J., *ECS Trans.* **1**(16), 61 (2005b).
Wieckowski, A., Fuel Cell Catalysis: A Surface Science Approach Hoboken. Wiley-Interscience, New Jersey (2009).
Yoon, W. and Weber, A. Z., *J. Electrochem. Soc.* **158,** B1007 (2011).
Zhao, Q. A., Majsztrik, P. and Benziger, J., *J. Phys. Chem. B* **115,** 2717 (2011).